2018

Molecular Dynamics Simulation Of Polymer Nanocomposites In Extreme Environments

Farzin Rahmani
University of Mississippi

MOLECULAR DYNAMICS SIMULATION OF POLYMER NANOCOMPOSITES IN EXTREME ENVIRONMENTS

A Dissertation
presented in partial fulfillment of requirements
for the degree of Doctor of Philosophy
in the Department of Chemical Engineering
The University of Mississippi

by

FARZIN RAHMANI

MAY 2018

ABSTRACT

In this dissertation, lower length scale phenomena associated with the responses of hybrid materials to harsh and extreme environments were studied. The goal of this research was to reveal the underlying mechanisms of damage mitigation in these materials and the role that interface, and relevant material component interactions play in the overall material response.

First, the thermal decomposition behavior of a technologically important material system, i.e., pristine graphene (PG) and graphene oxide (GO) reinforced poly(ethylene oxide) (PEO), was investigated using a reactive molecular dynamics simulation methodology. The simulations were performed in both non-isothermal (dynamic gravimetric) and isothermal modes of decomposition. Overall, the introduction of PG to the PEO system improves the thermal stability of the polymer in both decomposition modes. A delay in the temperature of the onset of decomposition in the non-isothermal mode and a nearly 60% increase in the activation energy of decomposition in the isothermal mode is observed for the PEO-PG system. This effect gets more pronounced with an increase in the PG concentration in the system. In contrast, introducing GO in the PEO system deteriorates the thermal stability of the polymer, even though, similar to the PG concentration effect, the thermal stability of the polymer is increased with increasing GO concentration.

Second, the effect of surface modification of polyoctahedral silsesquioxane (POSS) and its concentration in a polyimide (PI) matrix, as well as the effect of nanoparticle type (POSS, graphene, and carbon nanotube (CNT)) and the nanoparticle orientation in Gr and CNT nanoparticles in the PI matrix exposed to atomic oxygen (AO) bombardment were studied using a

reactive molecular dynamics simulation methodology. Among all systems, PI with randomly oriented CNTs or Gr nanoparticles gave, in general, the lowest mass loss, erosion yield, surface damage, AO penetration depth, and temperature. Grafting of the POSS nanoparticles with PI and the increasing the PI concentration lowers the erosion yield of the PI-POSS systems, with the effect of former being greater on the AO damage mitigation. The results of this fundamental study shed light on the lower length scale phenomena associated with AO damage mitigation in different PI-nanoparticle systems.

Third, the through-thickness temperature distribution and thermal conductivities of unprotected neat crosslinked epoxy, and protected epoxy/graphene, and epoxy/montmorillonite/graphene systems were investigated against lightning strike damage. It was inferred that the montmorillonite/graphene top coating has great potential to be used as a lightning strike damage protection measure for epoxy-based composite systems. A more thorough multi-physics (electrothermal) analysis of the montmorillonite/graphene system may further reveal its lightning strike damage mitigation efficiency.

TABLE OF CONTENTS

ABSTRACT ii

CHAPTER I 1

INTRODUCTION 1

CHAPTER II 4

CONFINEMENT EFFECTS ON THE THERMAL STABILITY OF POLY(ETHYLENE OXIDE)/GRAPHENE NANOCOMPOSITES: A REACTIVE MOLECULAR DYNAMICS SIMULATION STUDY 4

2.1. Abstract 4

2.2. Introduction 5

2.3. Computational Methods 7

2.3. Result and Discussion 11

2.3.1. Non-isothermal (dynamic thermogravimetric) simulation 11

2.3.2. Isothermal simulation 16

2.4. Conclusion 25

2.5. Acknowledgment 26

CHAPTER III 27

A REACTIVE MOLECULAR SIMULATION OF DAMAGE MITIGATION EFFICACY OF POSS-, GRAPHENE-, AND CARBON NANOTUBE-LOADED POLYIMIDE COATINGS EXPOSED TO ATOMIC OXYGEN BOMBARDMENT 27

3.1. Abstract 27

3.1. Introduction 28

3.3. Computational Details 30

3.4. Results and Discussion 35

3.5. Conclusion 48

3.6. Acknowledgment 50

CHAPTER IV 51

Thermal Analysis of Montmorillonite/Graphene Double-layer Coating as a Candidate Lightning Strike Protective Layer for Crosslinked Epoxy by Molecular Dynamics 51

4.1. Abstract 51

4.2. Introduction 51

4.3. Computational Details 53

4.4. Results and Discussion 56

4.5. Conclusions 59

4.6. Acknowledgements 60

CHAPTER V 61

CONCLUSIONS 61

LIST OF REFERENCES 64

LIST OF APPENDICES 75

APPENDIX A: ReaxFF Parameter Set of poly(ethylene oxide)/graphene nanocomposites 76

APPENDIX B: Polyimide Coatings Exposed to Atomic Oxygen Bombardment 84

B.1. Polymer Chain and Simulation Cell Size Effects 84

B.2. Relative Density Distributions 85

B.3. ReaxFF Parameter Set 87

VITAE 99

LIST OF FIGURES

Figure 2. 1. Snapshots of the initial equilibrium structures of a) PEO-2PG, b) PEO-4PG, and c) Confined PEO-2PG systems. Legend: carbon (black), hydrogen (green), and oxygen (red)..... 10

Figure 2. 2. Representative normalized number of PEO molecules and temperature as a function of simulation time. 13

Figure 2. 3. Evolution of major chemical species as a function of simulation time and temperature for a) Neat PEO, b) Confined PEO-2PG, c) PEO-4PG, and d) PEO-4GO systems. 15

Figure 2. 4. Snapshots of a) Neat PEO, b) Confined PEO-2PG, and c) PEO-4PG systems at 3,400 K (340 ps of non-isothermal simulation), where the size and location of the evolved macromolecular structures are shown. Legend: carbon (black), hydrogen (green), and oxygen (red)……..... 16

Figure 2. 5. Reaction rate data for the thermal decomposition of a) Neat PEO, b) PEO-2PG versus PEO-2GO, and c) PEO-4PG versus PEO-4GO systems. 18

Figure 2. 6. Mass distribution in a) Neat PEO, b) Confined PEO-2PG, c) PEO-2PG, d) PEO-2GO, e) PEO-4PG, and f) PEO-4GO systems at various temperatures after 40 ps of isothermal simulation…..... 23

Figure 2. 7. Through-thickness decomposition profiles for a) PEO-2PG system after 1 ps, b) PEO-2PG system after 40 ps, c) PEO-2GO system after 1 ps, and d) PEO-2GO after 40 ps of isothermal simulation at 2,400 K. The dotted lines indicate the approximate positions of the PG or GO sheets…. 24

Figure 2. 8. Isothermal evolution of major chemical species as a function of simulation time for a) Neat PEO and b) Confined PEO-2PG systems. 25

Figure 3. 1. Representative initial snapshots of the energy-minimized PI systems loaded with (a) aligned Gr and (b) aligned CNT nanoparticles. 33

Figure 3. 2. (a) Representative density evolution profiles for select systems during the equilibration of initial structures; (b)-(d) relative density (ρ/ρ_{bulk}) distribution in the simulation cells for representative systems after 2 ns of equilibration. 35

Figure 3. 3. Representative initial (t = 0 ps) and final (t = 35 ps) snapshots of the PI systems loaded with (a) pristine POSS (left: 15 wt% and right: 30 wt%), (b) PI-grafted POSS (left: 15 wt% and right: 30 wt%), (c) CNT (left: randomly oriented and right: aligned), and (d) Gr (left: randomly oriented and right: aligned). The details of the systems are given in Table 3.1. 35 ps of simulation is equivalent to a fluence of 10^{15} O atoms/cm^2. 38

Figure 3. 4. (a) Averaged normalized mass loss as a function of simulation time and fluence for the neat polyimide (PI) and loaded-PI systems with pristine and grafted POSS nanoparticles (pPOSS and gPOSS, respectively) at two nanoparticle concentrations of 15 wt% and 30 wt%; (b) radial distribution function showing the Si-Si intraparticle and interparticle atomic distances in the different PI-POSS systems. 39

Figure 3. 5. Averaged normalized mass loss as a function of simulation time and fluence for the neat polyimide (PI) and loaded-PI systems with grafted POSS (gPOSS), as well as randomly oriented and aligned Gr and CNT nanoparticles, at a concentration of 15 wt%. 41

Figure 3. 6. (a) Final snapshot of a layered hydrogen-terminated Gr system (black = carbon, silver = hydrogen) bombarded with atomic oxygen (AO) species (red), (b) final normalized mass density profile of the AO (material surface is located at z = 0 Å) in the layered Gr system, and (c) normalized mass loss as a function of simulation time and fluence for the layered Gr system bombarded with AO..... 42

Figure 3. 7. An example of the final normalized mass density profiles along the z-axis of the PI systems loaded with aligned graphene nanoparticles. The material surface is located at z = 0 Å. The damage propagation depth is shown by the arrow..... 46

Figure 3. 8. Representative final normalized mass density profiles of the atomic oxygen (AO) in (a) PI-POSS and (b) PI-Gr and PI-CNT systems. The material surface is located at z = 0 Å..... 47

Figure 3. 9. Representative temperature evolution profiles for the PI-POSS-15, PI-Gr-15, and PI-CNT-15 systems. The profiles for the PI systems loaded with pristine or PI-grafted POSS, as well randomly oriented or aligned Gr or CNT systems are very similar..... 48

LIST OF TABLES

Table 2. 1. Details of equilibrated initial systems after energy minimization and NVT simulation at 298 K and 1 atm. 9

Table 2. 2. Average temperature of the onset of thermal decomposition (extrapolated onset temperature) for the different systems 13

Table 2. 3. Activation energy (E_a) for the thermal decomposition of the various systems 19

Table 3. 1. Details of the nanoparticle-loaded polyimide (PI) systems 32

Table 3. 2. Average erosion yield[69] at different atomic oxygen exposure times 44

Table 3. 3. Average damage propagation depth (DPD) for different nanoparticle-loaded polyimide (PI) systems bombarded with AO species 46

CHAPTER I

INTRODUCTION

Environment is full of phenomena we can consider extreme, from our familiar phenomena on Earth's surface to those in the outer space:

- fluxes of radiation and particles from the Sun
- volcanic eruptions
- very high underground pressures and temperatures
- electromagnetic discharges, occurring in solar flares

Also, human activities usually create extreme environments. For instance, in

- high-powered lasers,
- high temperature engine and turbines,
- combustion engines, and
- industrial chemical plants.

The responses of materials to extreme environments, such as high stresses and strains, high or low temperatures, corrosive or oxidizing atmospheres, strong magnetic and electric fields, and intense photon or radiation fluxes result in phenomena that do not occur under normal conditions and can possibly cause failures that would limit the intended function of the materials in different applications. A critical understanding of the extreme environments and their implications for materials performance are of utmost importance in energy, military, and aerospace sectors. For

example, the design of smart materials capable of withstanding extreme conditions is the main focus in energy technologies for

- automobiles, satellites, and aircraft,
- electrical energy storage devices, such as fuel cells, solar cells, and batteries that have much longer lifetimes,
- electricity transmission and distribution systems that are more reliable and efficient,
- nuclear and stationary turbines, operating at higher temperatures with longer lifetimes, and
- distribution pipelines that are not subject to failures resulting from corrosion or other chemical reactions.

One of the key engineering materials are polymers and their composites. Because of their inherent limitations and not so reliable operation under extreme environments, these materials often need to be modified using a host of inclusions, such as nanomaterials. The addition of nanomaterials to engineering polymers often provides a means to improve the physico-chemical, electrical, thermal, and mechanical properties of the host polymer matrix. However, there are numerous levels of interaction between the material constituents that makes the prediction of the ultimate physical, chemical, mechanical, thermal, electrical, and other properties of the composite material very complex. In many cases, the interface between the different phases of the composite material, which often leads to the formation of an interphase region with a gradient of properties between those of the two phases, plays a major role in the ultimate response of the material system to external stimuli. These effects are often very difficult to elucidate or quantify through

experimental characterization efforts. Reactive molecular dynamics (MD) simulation is an invaluable tool to probe the lower length and time scale phenomena associated with the physico-chemo-mechanical changes of the material in response to external extreme and catastrophic conditions.

In this dissertation, we seek to elucidate the lower length scale phenomena associated with the response of hybrid materials to harsh and extreme environments. Our goal is to reveal the underlying mechanisms of damage mitigation in these materials and the role that interface, and relevant material component interactions play in the overall material response. This dissertation deals with the MD simulation of the damage mitigation in hybrid materials under three different extreme environments:

1- Temperature extremes: confinement effects on the thermal stability of poly(ethylene oxide)/graphene nanocomposites: a reactive molecular dynamics simulation study
2- Energetic flux extremes: damage mitigation efficacy of POSS-, graphene-, and carbon nanotube-loaded polyimide coatings exposed to atomic oxygen bombardment
3- Electro-thermal extremes: lightning strike protection of aircraft composite structures by multifunctional graphene/nanoclay bilayer coatings

CHAPTER II

CONFINEMENT EFFECTS ON THE THERMAL STABILITY OF POLY(ETHYLENE OXIDE)/GRAPHENE NANOCOMPOSITES: A REACTIVE MOLECULAR DYNAMICS SIMULATION STUDY

In this chapter, the decomposition of poly(ethylene oxide) loaded with different concentrations of pristine graphene and graphene oxide nano-platelets under extremely high temperature condition were investigated using reactive molecular dynamics simulation. The outcome of this research was published in Journal of Polymer Science Part B.

2.1. Abstract

Non-isothermal and isothermal decomposition of poly(ethylene oxide) (PEO) loaded with different concentrations of pristine graphene (PG) and graphene oxide (GO) nano-platelets were investigated using reactive molecular dynamics simulation. The onset of non-isothermal decomposition of the PG-loaded PEO system was the highest among all systems, suggesting that introducing PG to the polymer improves its thermal stability (an effect that increases with an increase in the PG concentration). At low concentration, introducing GO to the polymer brings about a deterioration of the thermal stability of the polymer consistent with experimental findings. On average, the activation energy for the isothermal decomposition of PG-loaded PEO system increases by 60% over that of the neat PEO system, while it decreases by 40% for the GO-loaded

PEO system. A time-dependent analysis of the through-thickness decomposition profile of the above systems reveals that the polymer confined between the PG sheets exhibit a higher thermal stability compared to the bulk polymer. However, an opposite effect is observed with the polymer confined between the GO sheets. The latter observation is attributed to accelerated polymer chain scission in confined regions due to the ejection of reactive hydroxyl radicals from the GO surface during the early stages of thermal decomposition.

2.2. Introduction

The addition of nanomaterials to engineering polymers often provides a means to improve the physico-chemical, electrical, thermal, and mechanical properties of the host polymer matrix.[1-3] However, there are numerous levels of interaction between the material constituents that makes the prediction of the ultimate physical, chemical, mechanical, thermal, electrical, and other properties of the composite material very complex.[4] In many cases, the interface between the different phases of the composite material, which often leads to the formation of an interphase region[5-8] with a gradient of properties between those of the two phases, plays a major role in the ultimate response of the material system to external stimuli. This is true since most of the polymer-nanoparticle interactions are mediated through this region. Moreover, in certain two-dimensional (2D) nanomaterials, such as graphene nano-platelets, nanoclays, etc., the intercalated polymer in the galleries of the nanomaterial may exhibit a different behavior than that of the "bulk" polymer due to "confinement" effects.[9, 10] These effects are often very difficult to elucidate or quantify through experimental characterization efforts.

Reactive molecular dynamics (MD) simulation is an invaluable tool to probe the lower length and time scale phenomena associated with the physico-chemo-mechanical changes of the material in response to external extreme and catastrophic conditions. Few researchers have used this tool

to investigate the thermal decomposition of polymers.[11-15] However, to the best of our knowledge, there are no reports on the reactive MD simulation of thermal decomposition in polymer composites. In this work, the non-isothermal and isothermal (dynamic thermogravimetric) behavior of poly(ethylene oxide) (PEO) reinforced with pristine graphene (PG) and graphene oxide (GO) nano-platelets are investigated using a reactive MD simulation, with focus on elucidating the effects of polymer confinement between the PG and GO nano-platelets. For reference, PEO-GO systems are of applied interest as solid-state flexible polyelectrolyte films[16] used in "wearable" solar cells.

Contrary to computational work, there are few experimental reports available on the PEO-graphene systems in literature. Lee et al.[17] prepared a PEO-functionalized graphene sheet (FGS) composite film by a solvent casting method. Based on their differential scanning calorimetry data, the FGS hindered the growth of PEO crystals. They further report on an improvement in the dynamic mechanical and electrical conductivity of PEO by incorporating FGS in the material formulation. Bai et al.[18] prepared PEO-chemically reduced graphene [PEO-(CR-G)] composites by an aqueous mixing method. At a CR-G amount of 2.6 vol%, the PEO-(GR-G) composite exhibits a high microwave-absorbing capacity, which the authors attribute to the presence of a large number of electrical pathways within the CR-G sheets. They argue that these electrical pathways effectively dissipate the microwave energy into heat. Mahmoud[19] reports on the morphology and physical properties of PEO-foliated graphene sheet (PEO-FGS) composites prepared by melt compounding and solvent mixing. The solvent-mixed PEO-FGS system was found to give a higher optical transparency in the visible region, a lower FGS percolation threshold for electrical conductivity, and a better mechanical performance (stress-strain response) than that of the melt-compounded PEO-FGS system. Wang et al.[20] investigated the heat storage capacity

of polyethylene glycol-GO (PEG-GO) system. The most recent work on the confinement effects in the thermal decomposition of polymer-graphite oxide systems was published by Barroso-Bujans et al.[21] They investigated the thermal stability of intercalated PEO in a PEO-GO system using a combination of X-ray diffraction, thermogravimetric analysis (TGA), and TGA-mass spectroscopy. Based on their findings, the addition of GO to PEO deteriorates the thermal stability of the PEO-GO composite.

Since the key mechanisms associated with the thermal stability of a technologically important class of polymer composites, i.e., PEO-PG and PEO-GO composite films, are poorly understood, the current work provides the necessary molecular insights for a better design of such systems. The methodology presented herein can be extended to other polymer composites.

2.3. Computational Methods

The structures of PEO, PG, and GO were created in BIOVIA Materials Studio® (v8.0). Ten monomer units, i.e., $-(CH_2\text{-}CH_2\text{-}O)-_n$ with n = 10, were selected for each PEO polymer chain. Hydrogen-terminated finite PG and GO sheets were created in the size of 30×30 $Å^2$. In the GO sheets, graphene was randomly functionalized with hydroxyl (-OH) and epoxide (-O-) groups on the surface and with carboxylic acid (-COOH) groups on the edges.[22, 23] The final oxygen to carbon (O/C) ratio for the GO sheets was 1:6. Next we created six different configurations of neat PEO and graphene-loaded PEO systems using the Amorphous Cell® module within Materials Studio. These configurations are given in Table 2.1 and consist of 1) a neat PEO system (designated as Neat PEO), 2) a PEO system with two PG sheets at a separation distance of 12 Å (PEO-2PG), 3) a PEO system with two GO sheets, 14 Å apart (PEO-2GO), 4) a PEO system with four PG sheets (all PG pairs at 12 Å separation distance), 5) a PEO system with four GO sheets

(all GO pairs at 14 Å separation distance), and 6) a confined PEO system between two PG sheets, 12 Å apart (Confined PEO-2PG). The distances between the graphene sheets were measured after the energy-minimization and subsequent equilibration of the initial structures by running an NPT simulation at atmospheric pressure and room temperature (298 K) using the COMPASS force field[24] with a time step of 1 fs and cutoff distance of 12 Å for a total simulation time of 3 ns. The coordinates of all PG sheet atoms were fixed for the Confined PEO-2PG structure during simulation. A schematic representation of the equilibrated PEO-2PG, PEO-2GO, and Confined PEO-2PG systems are given in Figure 2.1. Once created, the atomic coordinates of the initial structures were exported to LAMMPS,[25] where they were energy-minimized using the Polak-Ribiere version[26] of the Conjugate Gradient (CG) method.[27] All subsequent simulations were run using the reactive force field (ReaxFF) implemented in LAMMPS.[28, 29] ReaxFF is a highly transferable empirical interatomic potential that utilizes a bond-order formalism, similar to REBO[30] and MEAM-BO,[31] and polarizable charge descriptions to describe reactive and non-reactive interactions between atoms.[32] It is a suitable force field for the simulation of systems undergoing chemical reactions, such as thermal decomposition.[14] In the ReaxFF formalism, the total energy of the system is divided into partial energy contributions as:[32]

$$E_{\text{system}} = E_{\text{bond}} + E_{\text{angle}} + E_{\text{tors}} + E_{\text{over}} + E_{\text{vdW}} + E_{\text{Coulomb}} + E_{\text{specific}}, \quad (2.1)$$

where E_{bond} is the energy associated with bond formation between atoms, E_{angle} and E_{tors} are the energies associated with valence angle strain and torsional angle strain, respectively, E_{over} is an energy penalty term that prevents the over-coordination of the atoms, E_{vdW} and E_{Coulomb} are the dispersive and electrostatic energy contribution between all atoms, respectively, and E_{Specific} is a system-specific energy term that may include lone-pair, conjugation, hydrogen binding, and C_2

corrections.[32] More details on the ReaxFF formalism can be found in the work Chenoweth et al.[28] An excellent review of development, evolution, and future direction of ReaxFF is given by Senftle et al.[32] Since ReaxFF has been used in the past for the reactive simulation of polyethylene pyrolysis[33] and graphene decomposition due to hypervelocity atomic oxygen impact,[34] it is deemed suitable for the thermal decomposition simulations performed in this work. The ReaxFF parameter set herein were taken from the work of Chenoweth et al.[28] and are provided in the Appendix A for reference.

Once energy-minimized, the systems were equilibrated using an NVT simulation with a time step of 0.05 fs at 298 K for a total simulation time of 20 ps until the system temperatures were stabilized. The system temperature was controlled by the Berendsen thermostat.[35] Details of the equilibrated initial structures are given in Table 2.1.

Table 2. 1. Details of equilibrated initial systems after energy minimization and NVT simulation at 298 K and 1 atm.

System	Cell Size ($Å^3$)	Total No. of Atoms	No. of PEO Molecules	No. of Nanoparticles	Density (g/cm^3)
Neat PEO	31.3×31.3×31.3	7,290	48	0	1.15
Confined PEO-2PG[a]	37.0×32.0×12	2,328	21	2	-
PEO-2PG	33.0×33.0×82	9,960	126	2	1.21
PEO-2GO	36.2×36.2×83	11,136	139	2	1.20
PEO-4PG	33.2×33.2×83	9,768	111	4	1.26
PEO-4GO	33.1×33.1×82	9,240	97	4	1.24

[a] The *x*, *y*, and *z* coordinates of both PG sheet atoms were fixed.

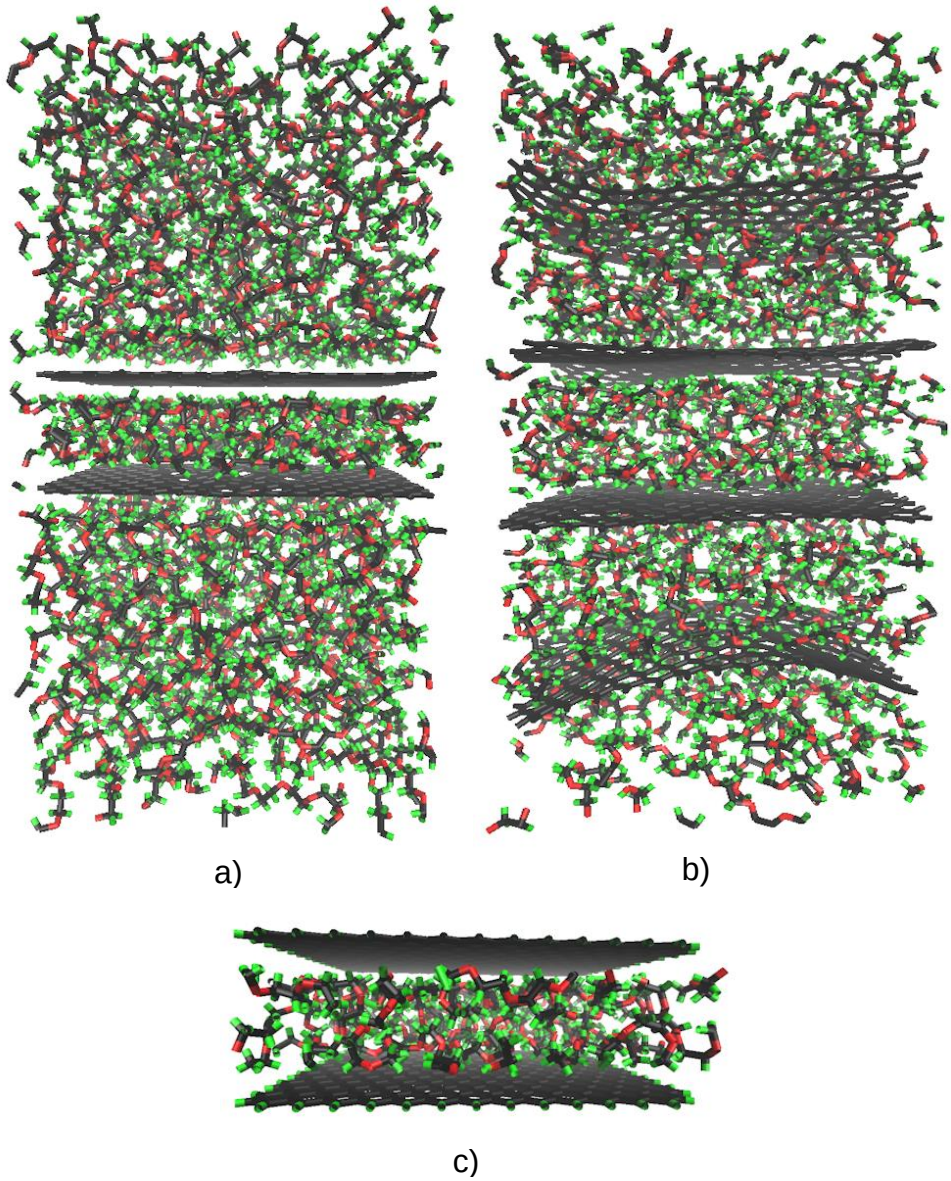

Figure 2. 1. Snapshots of the initial equilibrium structures of a) PEO-2PG, b) PEO-4PG, and c) Confined PEO-2PG systems. Legend: carbon (black), hydrogen (green), and oxygen

Next, we performed two sets of NVT simulations for all six systems, i.e., 1) non-isothermal (dynamic thermogravimetric) simulations starting from room temperature (298 K) up to 3,400 K with a temperature ramping rate of 16 K/ps for a total simulation time of 340 ps , and 2) isothermal simulations in the temperature range of 1,500-3,400 K with an increment of 100 K for a total

simulation time of 40 ps at each temperature increment. Again, the system temperature was controlled by the Berendsen thermostat. For both types of simulation, the long-range cut-off distance was 12 Å. In this work, the time step was fixed at 0.05 fs for all simulations performed at low and high temperatures, even though some researchers may select different times steps for different portions of their simulations because of computational convenience.[14] To reduce statistical noise, the non-isothermal simulations were repeated twice using different initial system configurations and the relevant data were averaged over the three simulations.

2.3. Result and Discussion

2.3.1. Non-isothermal (dynamic thermogravimetric) simulation

In Figure 2.2, representative normalized number of PEO molecules and temperature are given as a function of simulation time. At each time increment, the total number of the PEO molecules in the system is normalized with respect to the original number of PEO molecules at room temperature. To elucidate the thermal stability, the average temperature of the onset of the thermal decomposition for the different systems (averaged over three simulations with different initial configurations, as outlined in the Computational Method section) are compared in Table 2.2. In this table, the extrapolated onset temperatures were calculated using the method outlined in ASTM D 3418-15, where the intersection of two lines drawn tangent to the curve before and after the decomposition onset is reported as the temperature of the onset of thermal decomposition. As seen in Table 2.2, with the introduction of PG to the PEO system at low PG concentration, a slight increase in the decomposition onset temperature is observed for the PEO-2PG system (720 ± 8 K) versus that of the Neat PEO system (700 ± 8 K). However, introducing GO to the PEO system (PEO-2GO) causes a 5-10% drop in the decomposition onset temperature (650 ± 20 K) compared

to the Neat PEO system. Based on our observations, this drop in the thermal stability of the PEO-2GO system is attributed to the partial chemical decomposition of the functional groups on the GO surface, resulting in the evolution of both reactive (free radical) and non-reactive chemical species, such as OH, CHO, CO, CO_2, H_2O, and COOH. The free radicals further react with the PEO molecules, causing an early onset of the polymer decomposition. For reference, the initial polymer chain decomposition is initiated by the attack of hydroxyl radicals on the PEO. The chemistry of this reaction is similar to that observed for the thermo-oxidative decomposition of PEO as reported by Yang et al.[36] In an experimental study performed by Barroso-Bujans et al.[21] for an intercalated PEO-graphite oxide system versus neat PEO, an earlier onset of decomposition for the PEO-graphite oxide system is reported. This experimental observation is consistent with our simulation results. It should, however, be noted here that the thermogravimetric data obtained through MD simulations do not necessarily compare to the experimental data since the temperature ramping rate during simulations is an order of magnitude faster than that of the experiments. With an increase in the PG concentration, an improvement in the thermal stability of the PEO-PG system is observed over that of the neat PEO (Table 2.2). While a similar trend is observed for the PEO-GO system (Table 2.2), the thermal stability of this system is still below that of the neat PEO. These observations are closely related to the PEO confinement in PG and GO, which will be discussed in detail later. Based on our observations, an improved thermal stability of PEO is achieved when it is confined between two PG sheets compared to that of the Neat PEO system (Table 2.2). As seen in Table 2.2, the decomposition onset temperature for the Confined PEO-2PG system (780 ± 10 K) is about 80 K higher than that of the Neat PEO system (700 ± 8 K) and on par with that of the PEO-4PG system.

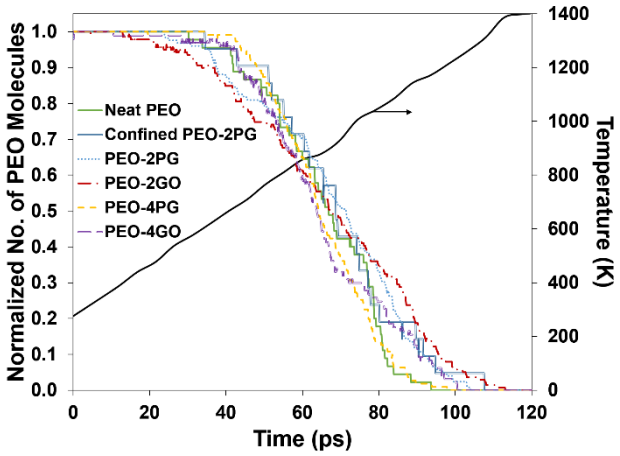

Figure 2. 2. Representative normalized number of PEO molecules and temperature as a function of simulation time.

Table 2. 2. Average temperature of the onset of thermal decomposition (extrapolated onset temperature) for the different systems

System	Neat PEO	Confined PEO-2PG	PEO-2PG	PEO-2GO	PEO-4PG	PEO-4GO
Temperature (K)	700	780	720	650	770	680
St. Dev.[a]	8	10	8	20	5	6

[a] Standard deviation

In Figure 2.3, the evolution of major chemical species, i.e., the polymer, CH_2O, C_2H_4, CHO, H_2O, CH_4, and H_2 are given as a function of simulation time (and temperature) for the Neat PEO, Confined PEO-2PG, PEO-4PG, and PEO-4GO systems. The ratio of CH_2O to C_2H_4 generated during the thermal decomposition of Confined PEO-2PG system (Figure 2.3b) is less than that of the Neat PEO system (Figure 2.3a). This suggests that the dominant decomposition mechanism for the polymer when confined between two PG sheets is chain scission. This point is revisited again when the isothermal decomposition data are presented later. While the total number of PEO molecules in the PEO-4GO system is less than that of the PEO-4PG system (Table 2.1), a larger

number of CH_2O and CHO molecules are formed for the former system than for the latter (Figures 3c and 3d). The initial system decomposition (up to about 100 ps or 1200 K) is characterized by the polymer chain scission events. Above this point, the build-up of CH_2O is observed for both systems, followed in intensity by C_2H_4, CHO, H_2O, CH_4, and H_2. Between 2,000 and 2,500 K, a secondary reaction occurs for the CH_2O, CHO, and C_2H_4 species and, hence, their concentration in the systems start to drop (Figure 2.3). These secondary reactions are believed to be caused by an increase in the concentration of free radicals in the systems at high temperatures, which result in an increase in the chemical attack to stable molecules.[14] During the non-isothermal simulation, GO partially disintegrates, i.e., its surface functional group decompose, at temperatures <600 K, while the PG disintegration starts at higher temperatures (>1500 K). Moreover, formation of an oxygenated macromolecular structure is observed at high temperatures (above 2,000-2,500 K). Examples of these macromolecular structures are shown for the Neat PEO, PEO-4PG, and Confined PEO-2PG systems at 3,400 K (340 ps of non-isothermal simulation) in Figure 2.4.

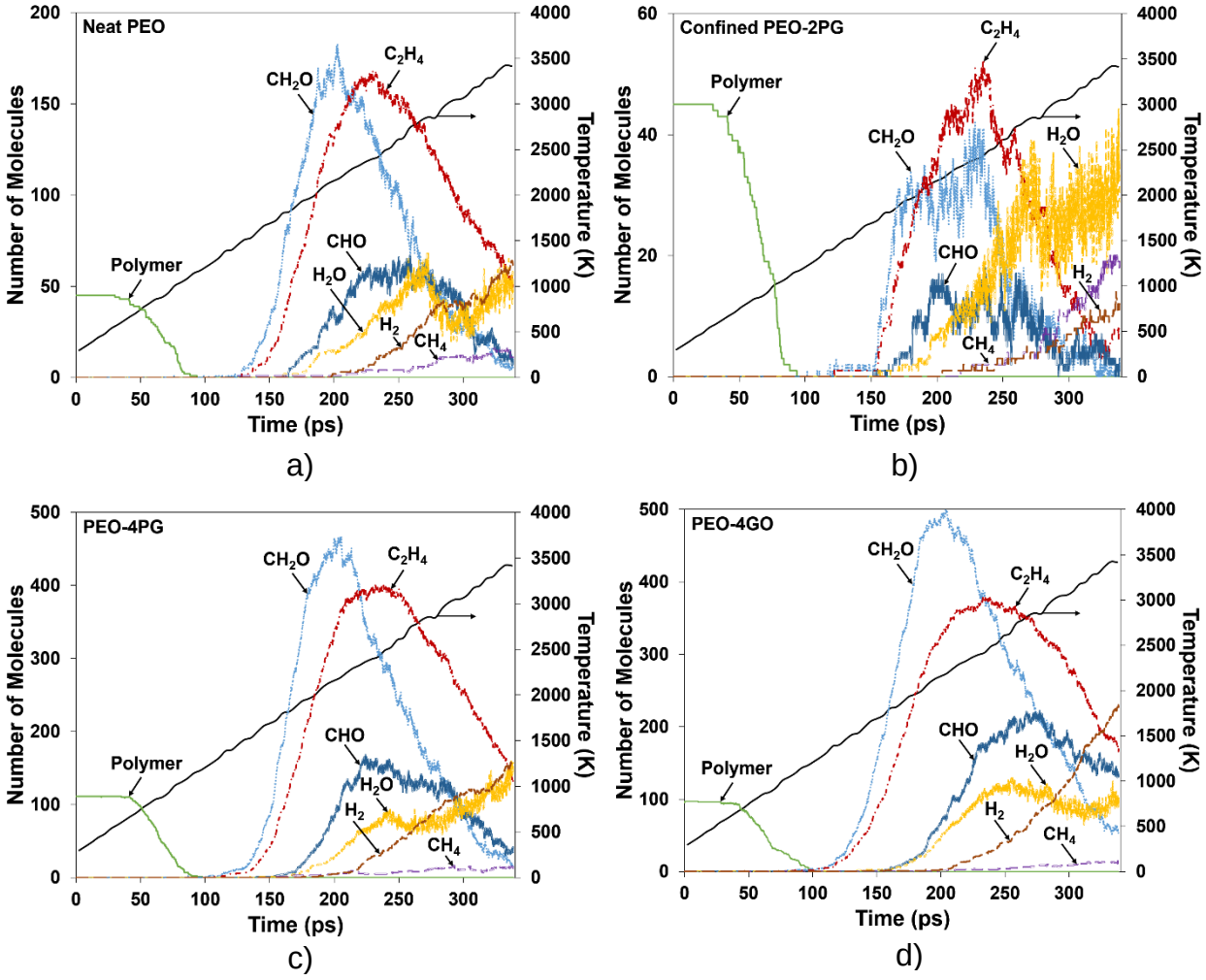

Figure 2. 3. Evolution of major chemical species as a function of simulation time and temperature for a) Neat PEO, b) Confined PEO-2PG, c) PEO-4PG, and d) PEO-4GO

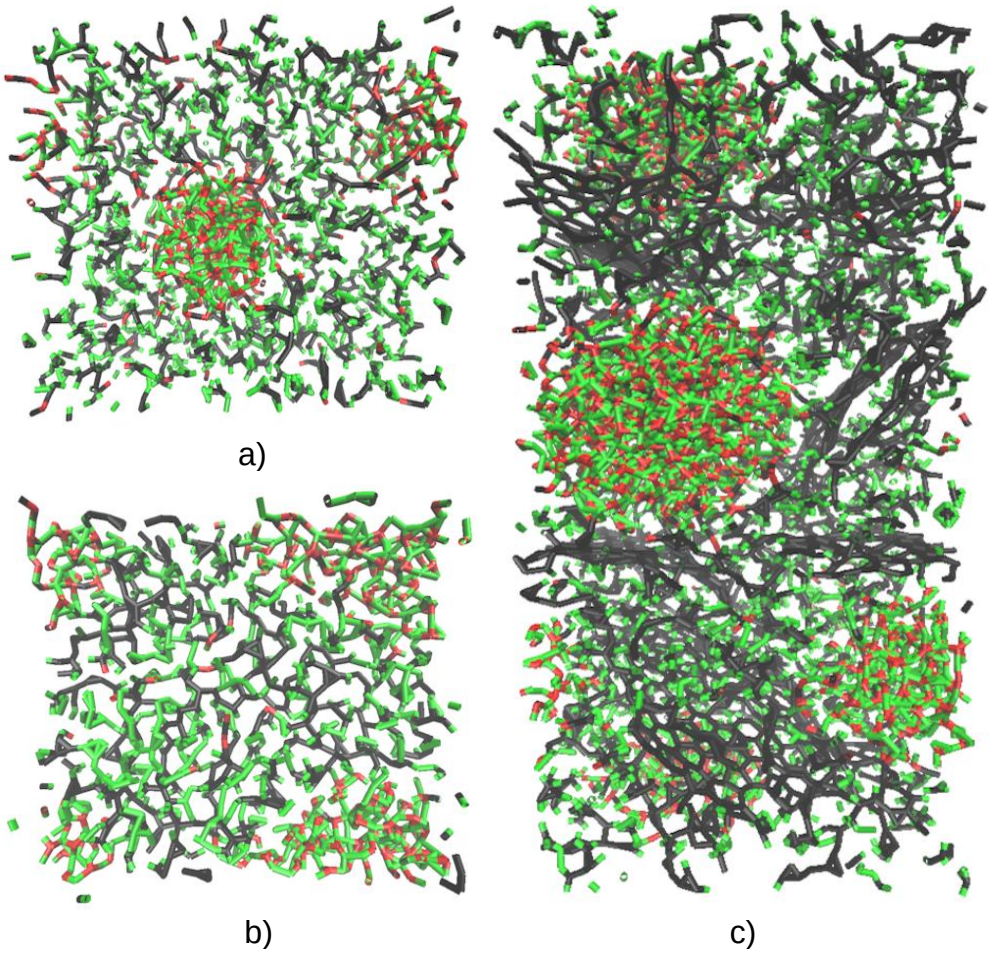

Figure 2. 4. Snapshots of a) Neat PEO, b) Confined PEO-2PG, and c) PEO-4PG systems at 3,400 K (340 ps of non-isothermal simulation), where the size and location of the evolved macromolecular structures are shown. Legend: carbon (black), hydrogen (green), and oxygen (red).

2.3.2. Isothermal simulation

Isothermal reactive simulations were run, as outlined in the previous section, to determine the first-order kinetics of thermal decomposition[21] in the different PG- and GO-reinforced PEO systems. The Arrhenius equation for the reaction rate constant (k) is given as

$$k = Ae^{\frac{-E_a}{RT}} \text{ or} \tag{2.2}$$

$$\ln(k) = \frac{-E_a}{R} T^{-1} + \ln(A), \tag{2.3}$$

where A is the pre-exponential (frequency) factor, E_a is the activation energy, and R is the universal gas constant. The reaction rate constant for the different systems was calculated using the following formula[11] for the dominant species generated during the isothermal decomposition of the PEO chains, similar to the methodology employed by Chenoweth et al.:[14]

$$k = \frac{n_{(CH_2O)_s}}{n_{(CH_2O)_p} \cdot t}, \tag{2.4}$$

where $n_{(CH_2O)_s}$ is the number of single CH_2O species evolved during the thermal decomposition, $n_{(CH_2O)_p}$ is the number of CH_2O species within the backbone of the original PEO chains, and t is the simulation time. The reaction rate data for the different systems, their respective linear fits, and coefficients of determination are shown in Figure 2.5. Finally, the calculated activation energies are given in Table 2.3. Since the time scales in an MD simulation are much smaller than the experimental and, hence, the temperature range for observing thermal decomposition events are much broader, the activation energy data in Table 2.3, which were obtained for data at high temperatures (> 1,000 K), do not compare to the experimental values. For a similar PEO-GO system,[21] the upper limit of decomposition temperature is typically less than 1,000 K. Nevertheless, the activation energy data are used for comparing between the thermal decomposition of the different systems.

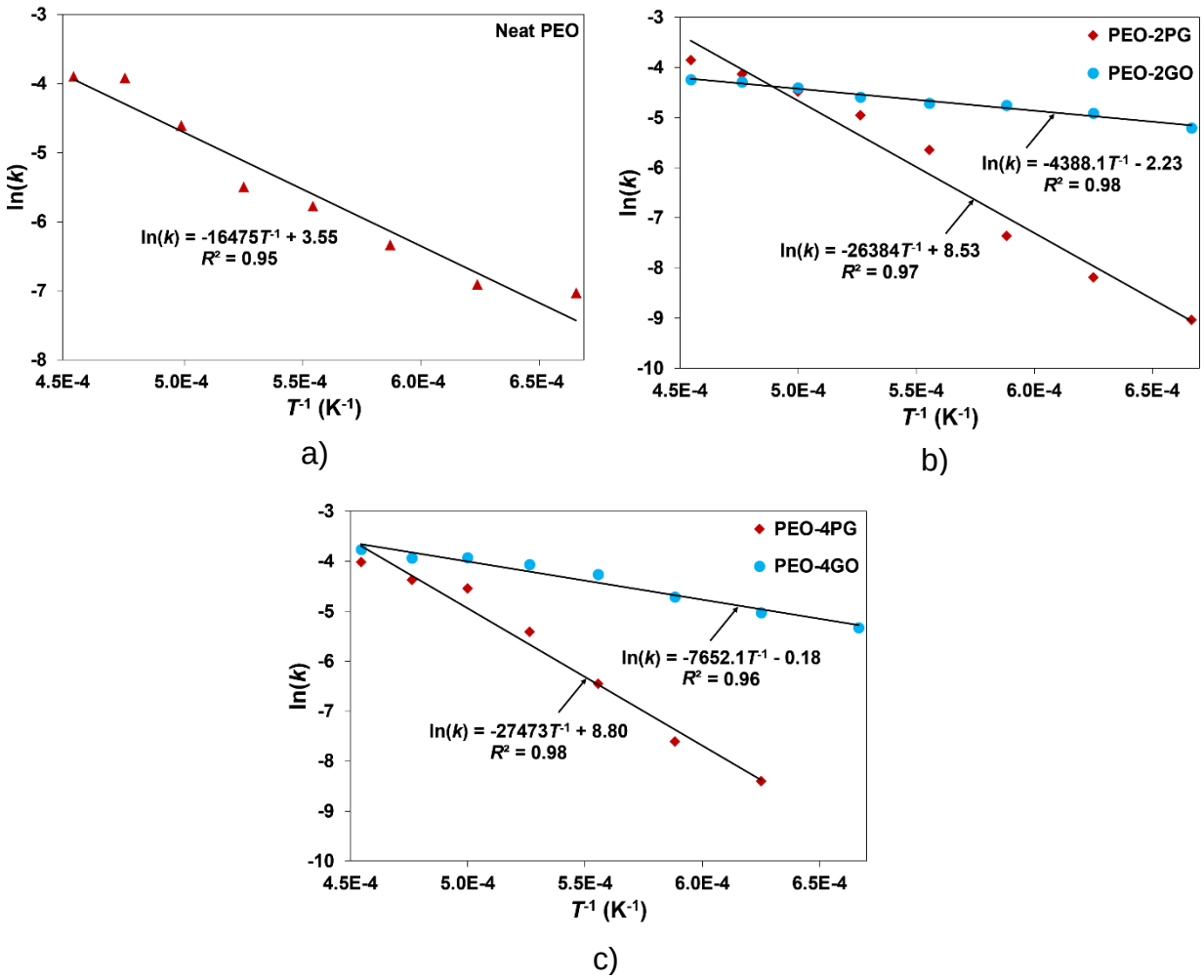

Figure 2. 5. Reaction rate data for the thermal decomposition of a) Neat PEO, b) PEO-2PG versus PEO-2GO, and c) PEO-4PG versus PEO-4GO systems.

Table 2. 3. Activation energy (E_a) for the thermal decomposition of the various systems

System	E_a (kcal/mol)
Neat PEO	32.74
PEO-2PG	52.43
PEO-4PG	54.59
PEO-2GO	8.72
PEO-4GO	15.21

As evident from Table 2.3, the activation energies for thermal decomposition of the PEO-PG systems are higher than those of the Neat PEO and PEO-GO systems. This observation, which is similar to that made for the non-isothermal simulations, indicates that an improvement in the thermal stability of PEO is achieved by introducing PG to the system, an effect that increases with increasing PG concentration (Table 2.3). Moreover, the occurrence of significantly lower activation energies for the PEO-GO systems versus that of the Neat PEO (Table 2.3) is an indication that the GO addition to the polymer deteriorates its thermal stability, even though increasing the GO concentration leads to a rise in the activation energy. Similar observations have been made by Barroso-Bujans et al.[21] regarding the activation energy differences between PEO-PG and PEO-GO systems.

To explain the above observations, a comparison is made between the mass distribution of the different systems at temperatures of 1,500, 2,000, and 2,500 K after 40 ps of isothermal simulation in Figure 2.6 (the dominant chemical species formed during the polymer decomposition are marked in Figure 2.6a). As seen in this figure, larger number of PEO chains (molecular mass of 442 g/mol) are present in the PEO-PG systems at 1,500 K (Figures 6c and 6e) versus those of the

neat PEO system (Figure 2.6a). In the PEO-GO systems (Figures 6d and 6f), the polymer chains are essentially non-existent. This observation confirms the fact that thermal stability of PEO is improved by the addition of PG and is deteriorated by the addition of GO. Data in Figure 2.6b suggest that the thermal stability of PEO confined between the PG sheets is significantly improved at all temperatures. In comparing the PEO-PG (Figures 6c and 6e) and PEO-GO systems (Figures 6d and 6f), a higher intensity is observed for the formation of CHO species in the latter, which is also higher than that of the Neat PEO system (Figure 2.6a). This is an indication of the thermo-oxidative decomposition of the polymer in the PEO-GO system.

To better elucidate the PEO confinement effect, a through-thickness decomposition profile is given in Figure 2.7 for the PEO-2PG and PEO-2GO systems at a representative temperature of 2,400 K. In this figure, each data point represents a specific molecule (originally present or evolved during the isothermal decomposition), the mass of which has been normalized with respect to the mass of the PEO chain. Moreover, the *z*-coordinate of the center of mass of the molecule in the normalized *z* dimension of the simulation box is given as the abscissa. As seen in this figure, the onset of thermal decomposition occurs after 1 ps in the "bulk" region of the system (Figure 2.7a), while the "confined" region between the two PG sheets is still intact. After 40 ps of isothermal simulation, there are still PEO chains in the confined region (Figure 2.7b), indicating an improved thermal stability of the polymer in this region compared to the bulk. This observation can be explained based on two related mechanisms. According to the first mechanism, the polymer free volume decrease in the confined region leads to a reduced occurrence of "hot spots" in the confined polymer during temperature rise, which further results in a reduced local decomposition rate for the polymer.[37] According to the second mechanism, the PEO chains in the confined and interfacial regions are immobilized on the PG surfaces during thermal decomposition. These

immobilized chains undergo intermittent scission and recombination reactions, thereby limiting the number of available free radicals for continued chain scission reactions in the confined region. In the case of the Neat PEO system, the polymer chain scission reactions during thermal decomposition produce highly mobile free radicals that further produce CH_2O species when attacking other chains. This observation is shown in Figure 2.8. In comparing the Neat PEO (Figure 2.8a) and Confined PEO-2PG (Figure 2.8b) systems undergoing an isothermal decomposition at 3,400 K, the formation of larger number of CH_2O species is evident for the former. Another decomposition reaction is the thermally induced cleavage reactions that produce C_2H_4 species. At longer simulation times, the chains start to fully disintegrate and the frequency of small-molecule free radical formation is increased. These molecules diffuse away from the PG surfaces and cause thermal decomposition in the confined region. While Barroso-Bujans et al.[21] argue that the thermal stability of graphene (G)-reinforced PEO is inferior to that of Neat PEO, our results in this work indicate that PG actually improves the thermal stability of PEO as evident from both non-isothermal and isothermal simulations. The discrepancy between two sets of results are due to the fact that the graphene platelets used in the work of Barroso-Bujans et al. is not pristine, but has oxygenated groups on the surface, resembling those of GO.

In contrast to the PEO-2PG system, the decomposition profile of the PEO-2GO system after 1 ps of isothermal simulation (Figure 2.7c) shows a more severe thermal decomposition in the interfacial and confined regions versus that of the bulk region, consistent with the findings of Barroso-Bujans et al.[21] At 40 ps, the system is uniformly decomposed (Figure 2.7d). The ejection of reactive small chemical species, such as OH, from a GO sheet during thermal decomposition causes a more severe PEO chain scission in the neighborhood of the GO sheet[21] as evidenced in Figure 2.7c. When the GO (or PG) concentration is increased in the system, the

free radicals formed in the confined regions are barred from diffusing to the bulk by the graphene sheets and, therefore, the cumulative effect of such a restricted movement of the free radicals is an improved non-isothermal and isothermal stability of the bulk PEO. Similar arguments have been made by Barroso-Bujans et al.[21]

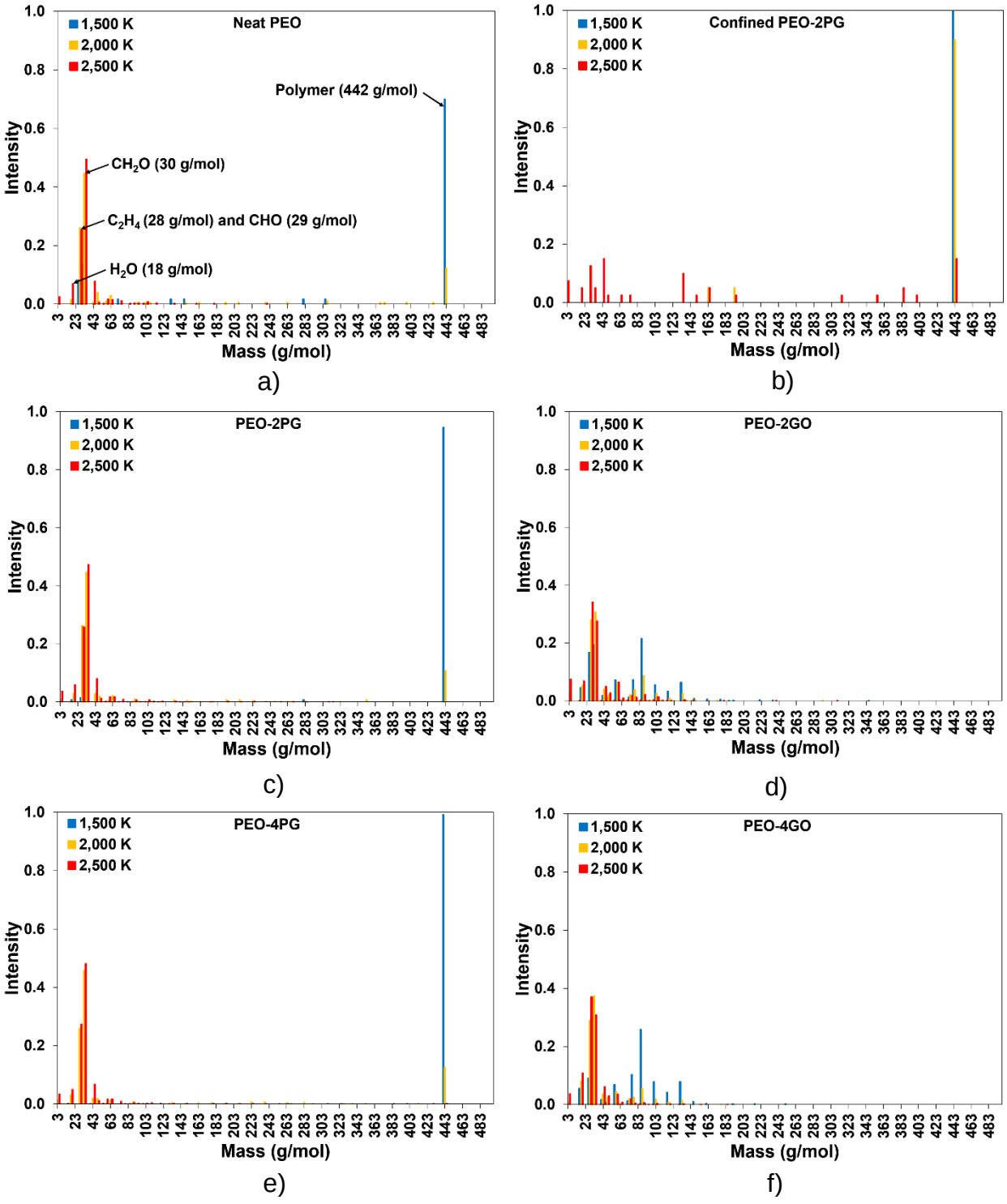

Figure 2. 6. Mass distribution in a) Neat PEO, b) Confined PEO-2PG, c) PEO-2PG, d) PEO-2GO, e) PEO-4PG, and f) PEO-4GO systems at various temperatures after 40 ps of isothermal simulation.

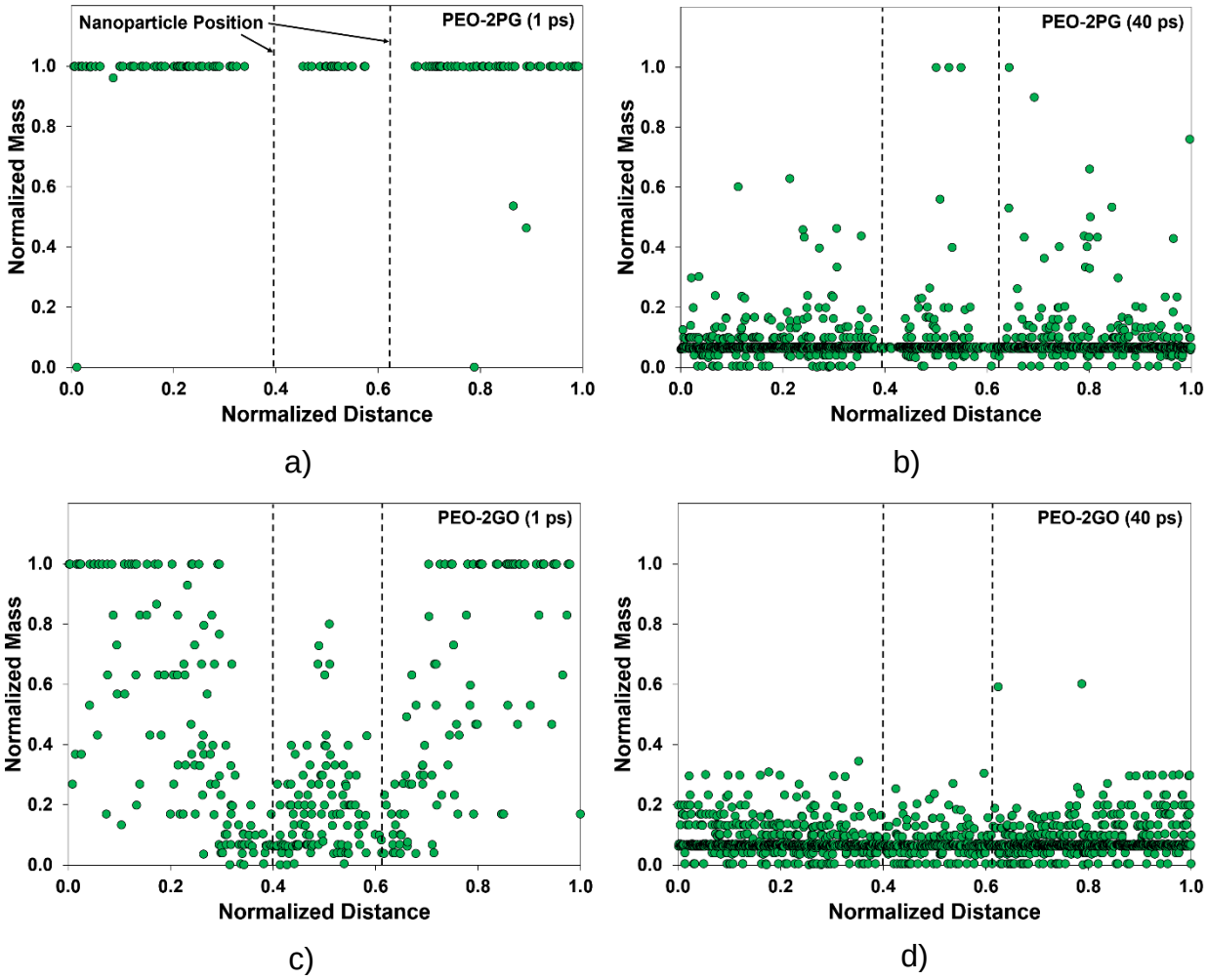

Figure 2. 7. Through-thickness decomposition profiles for a) PEO-2PG system after 1 ps, b) PEO-2PG system after 40 ps, c) PEO-2GO system after 1 ps, and d) PEO-2GO after 40 ps of isothermal simulation at 2,400 K. The dotted lines indicate the approximate positions of the PG or GO sheets.

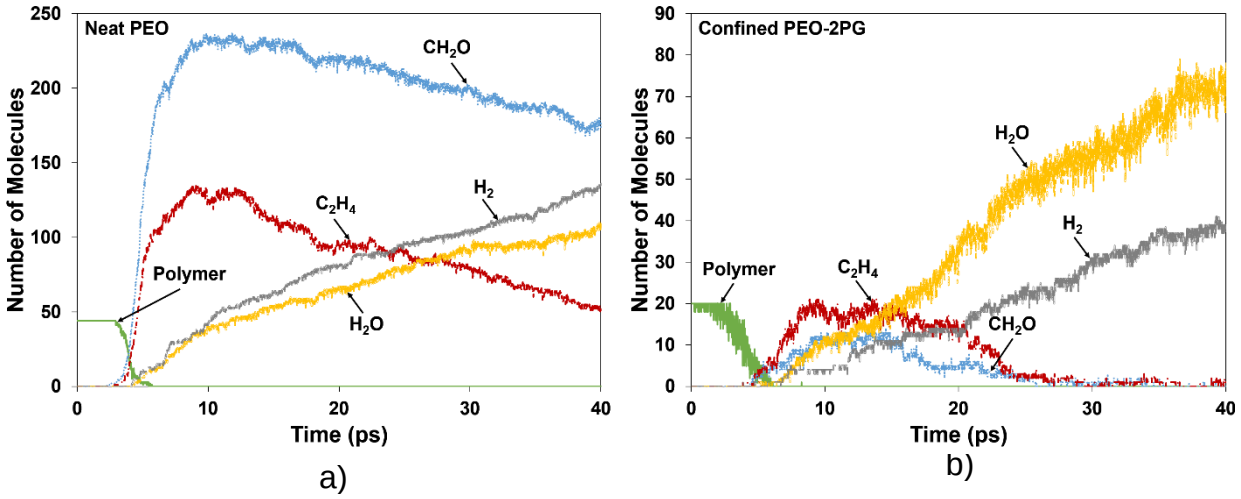

Figure 2. 8. Isothermal evolution of major chemical species as a function of simulation time for a) Neat PEO and b) Confined PEO-2PG systems.

2.4. Conclusion

Incorporation of nanoparticles in polymers is often thought to improve the thermal stability of the host polymer matrix. However, this is not always the case as the thermal behavior of the nanoparticle-reinforced polymer is strongly governed by the chemistry of the nanoparticle surface and its physico-chemical interactions with the polymer molecules. In this work, the thermal decomposition behavior of a technologically important material system, i.e., pristine graphene (PG) and graphene oxide (GO) reinforced poly(ethylene oxide) (PEO), was investigated using a reactive molecular dynamics simulation methodology. This specific material system is of interest in the development of flexible solid-state polyelectrolyte films for "wearable" solar cells. The simulations were performed in both non-isothermal (dynamic gravimetric) and isothermal modes of decomposition. Overall, the introduction of PG to the PEO system improves the thermal stability of the polymer in both decomposition modes. A delay in the temperature of the onset of decomposition in the non-isothermal mode and a nearly 60% increase in the activation energy of decomposition in the isothermal mode is observed for the PEO-PG system. This effect gets more

pronounced with an increase in the PG concentration in the system. In contrast, introducing GO in the PEO system deteriorates the thermal stability of the polymer, even though, similar to the PG concentration effect, the thermal stability of the polymer is increased with increasing GO concentration.

An investigation of the PEO confinement between the PG and GO nano-platelets reveals that thermal stability of the polymer is improved in the confined region versus that of the bulk region of the polymer. This effect is attributed to the immobilization of the polymer chains on the surfaces of the PG sheets, reduced free volume, and finally reduced occurrence of "hot spots" during thermal decomposition. In contrast, the PEO thermal stability is significantly deteriorated in the confined region between two GO sheets versus that of the bulk region of the polymer. This observation is rooted in the fact that polymer chain scission during temperature rise is accelerated in the neighborhood of the GO sheets because of the evolution of highly reactive hydroxyl radicals that immediately attack the polymer chains. At higher GO (and PG) concentrations, the free radicals formed in the confined regions are restricted from moving to the bulk and, hence, improved non-isothermal and isothermal stability of the bulk PEO is observed.

The results of this study shed light on the mechanisms of thermal decomposition in the PEO-PG and PEO-GO hybrid systems and provide insight on the polymer confinement effects on its thermal stability.

2.5. Acknowledgment

The authors wish to acknowledge Jason G. Hale, Director of the Office of Research and Sponsored Programs at the University of Mississippi, and Alexander H. D. Cheng, Dean of the School of Engineering at the University of Mississippi, for their support of this work

CHAPTER III

A REACTIVE MOLECULAR SIMULATION OF DAMAGE MITIGATION EFFICACY OF POSS-, GRAPHENE-, AND CARBON NANOTUBE-LOADED POLYIMIDE COATINGS EXPOSED TO ATOMIC OXYGEN BOMBARDMENT

In The second part, a reactive molecular dynamics simulation was employed to compare between the damage mitigation efficacy of pristine and polyimide (PI)-grafted polyoctahedral silsesquioxane, graphene, and carbon nanotubes in a polyimide matrix exposed to extreme energetic atomic oxygen flux. The outcome of this research was published in Journal of Applied Materials and Interfaces.

3.1. Abstract

A reactive molecular dynamics simulation was employed to compare between the damage mitigation efficacy of pristine and polyimide (PI)-grafted polyoctahedral silsesquioxane (POSS), graphene (Gr), and carbon nanotubes (CNTs) in a PI matrix exposed to atomic oxygen (AO) bombardment. The concentration of POSS and the orientation of Gr and CNT nanoparticles were further investigated. Overall, the mass loss, erosion yield, surface damage, AO penetration depth, and temperature evolution are lower for the PI systems with randomly oriented CNTs and Gr or PI-grafted POSS compared to those of the pristine POSS or aligned CNT and Gr systems at the same nanoparticle concentration. Based on experimental early degradation data (before the onset of nanoparticle damage), the amount of exposed PI, which has the highest erosion yield of all

material components, on the material surface is the most important parameter affecting the erosion yield of the hybrid material. Our data indicate that the PI systems with randomly oriented Gr and CNT nanoparticles have the lowest amount of exposed PI on the material surface; therefore, a lower erosion yield is obtained for these systems compared to those of the PI systems with aligned Gr and CNT nanoparticles. However, the PI/grafted-POSS system has a significantly lower erosion yield than the PI systems with aligned Gr and CNT nanoparticles, again due to a lower amount of exposed PI on the surface. When comparing the PI systems loaded with PI-grafted POSS versus pristine POSS at low and high nanoparticle concentrations, our data indicate that grafting the POSS and increasing the POSS concentration lower the erosion yield by a factor of about 4 and 1.5, respectively. The former is attributed to a better dispersion of PI-grafted POSS versus that of the pristine POSS in the PI matrix, as determined by the radial distribution function.

3.1. Introduction

Hypervelocity atomic oxygen (AO) bombardment of satellite and other spacecraft positioned in or flying through the low Earth orbit (LEO) is a serious problem for their structural integrity and long-term operational safety. AO, which has a relative velocity of 7-8 km/s upon impact with moving spacecraft, rapidly oxidizes and degrades the exposed surfaces of polymers that are typical matrices for spacecraft structural composites.[38, 39] The result of erosion due to AO bombardment is a loss of material thickness, a textured surface morphology, and propensity to catastrophic material failure.[38] One protective measure to mitigate the AO bombardment damage is to use nanoparticle-enhanced coatings,[40] prepared by incorporating nanoparticles such as polyoctahedral silsesquioxanes (POSS),[41-48] POSS-TiO_2,[49] carbon nanotubes

(CNTs),[50] CNT-POSS,[51] graphene (Gr),[52-55] ZnO nanowires,[56] ZrO_2,[57] and boron nitride nanosheets (BNNS)[58] in an aerospace-grade polymer matrix, such as polyimide (PI). The nano-enhanced coatings typically exhibit significantly lower erosion yield[59] than those of the neat polymers. However, whenever these coatings are electrically insulating, such as a PI-POSS coating, they may become charged during exposure to space plasma, thereby causing hazardous electrostatic discharge.[51] Therefore, a secondary objective in protecting the spacecraft is often to shield the structures and electronics to electrostatic discharge hazards by incorporating nanoparticles such as Gr and CNT, which are electrically conductive. It is noteworthy to mention that the AO damage mitigation efficacy of Gr and CNT has received much less attention than that of POSS. One objective in this work is to fill this scientific gap and provide relevant molecular insights.

While there are numerous theoretical and experimental studies published in literature on the subject of AO attack and its mitigation by nanoparticle-enhanced polymer coatings,[40, 60, 61] relevant publications for computational studies are scarce. Srinivasan and van Duin[62] performed a reactive molecular dynamics (MD) simulation of hyperthermal AO collisions with Gr to elucidate a possible chemical degradation of the Gr nanoparticle. They report the removal of an O_2 molecule from the surface of the Gr sheet upon the AO impact through an Eley–Rideal-type reaction mechanism. Moreover, the Gr sheet buckles along its diagonal. Rahnamoun and van Duin[63] investigated the chemistry of degradation in Kapton®, Teflon®, POSS, and amorphous silica exposed to AO attack. Through their reactive MD simulation, they found that Kapton is less resistant to the AO attack than Teflon. Moreover, amorphous silica exhibits the highest durability among the materials simulated before silicon starts to oxidize. In a recent study by Zeng et al.,[46] the role of trifluoropropyl-modifed POSS (FP-POSS) in mitigating the AO impact damage in a

polyvinylidene fluoride (PVDF) matrix was studied using a reactive MD simulation. The incorporation of FP-POSS into PVDF was found to significantly enhance the durability of PVDF against AO attack, as evidenced by a reduced temperature rise, mass loss, and erosion yield of the polymer nanocomposite. The erosion will not take place until the number of AO species reaches a specific threshold value. The late onset of erosion is attributed to the stable cage-like Si-O frames in the FP-POSS molecules.

Most of the recent studies on the improvement of nanoparticle-assisted AO damage durability of polymer composites have been limited in their scope. A thorough comparison between the damage mitigation efficacy of various nanoparticles, especially Gr and CNT, have been largely overlooked. Moreover, to the best of our knowledge, the effect of nanoparticle alignment in Gr and CNT nanoparticles on the durability of the polymer nanocomposite to the AO attack has not been studied. It is, therefore, our aim in this work to compare the AO damage mitigation efficacy of pristine and PI-grafted POSS, Gr, and CNT nanoparticles in a PI matrix, considering the latter two nanoparticles' orientation. In addition, the effect of POSS grafting and concentration on the AO damage mitigation is examined in the PI/POSS systems.

3.3. Computational Details

The computational methodology used herein is adapted from the work of Rahnamoun and van Duin.[63] Models of the imide monomer (an idealized representation of PI),[63] pristine POSS (the cage structure associated with $(SiO_{1.5})_n$ n = 8),[63] PI-grafted POSS,[63] Gr (hydrogen-terminated, 20×22 $Å^2$), and CNT (single-walled (6,6) structure with a length of 25 Å) were created in BIOVIA Materials Studio® (v8.0). Since reactive MD simulation is computationally expensive

and the focus in this work is not on the nanoparticle size effects, the CNT and Gr nanoparticle sizes were selected such that they would be appropriate for the simulation cells created (Table 3.1). Next, nine different systems, as listed in Table 3.1, were packed in a 3D-periodic simulation cell and energy-minimized using the Conjugate Gradient method.[27] The crosslinking of PI was not considered in this work, as it is anticipated that its effect on the AO damage mitigation is small since the structures are not under external load. This approach is consistent with similar work published in the past.[63] In the PI-Gr-Aligned-15 and PI-CNT-Aligned-15 systems (Table 3.1), Gr sheets and CNTs were placed perpendicular to the AO bombardment direction (Figure 3.1). For each system, an initial NPT (constant number of atoms, N; constant pressure, P; constant temperature, T) simulation was run for a total of 2 ns at room temperature (298 K) and atmospheric pressure using the COMPASS force field[24] within Materials Studio. The system temperature and pressure were controlled with the Nosé-Hoover thermostat and barostat,[64] respectively. The simulations were run until the system densities were equilibrated at about 1.9-2.0 g/cm^3 for the PI-POSS systems and 1.6-1.8 for the PI-Gr and PI-CNT systems, respectively (Figure 3.2a). By investigating the density evolution profiles for select systems in Figure 3.2a, it is evident that the systems were adequately equilibrated after 2 ns of NPT simulation. Moreover, by investigating the relative density distributions (ρ/ρ_{bulk}) of the select systems in the *x*, *y*, and *z* directions of their respective simulation cells (Figures 2b-2d), a fluctuation of about 4-7% is observed, indicating that all structures are well-formed after 2 ns of simulation. For reference, the remaining relative density data are given in the Appendix B. To improve the statistical sampling, three separate simulations were run for each system and the relevant data were averaged over all three simulations.

It has to be emphasized here that, similar to any MD simulation study of complex material systems, size effects may have some influence on the obtained results. While not within the scope of this work, a side study was performed on the Neat PI system to evaluate the extent of such size effects. The relevant procedure and results are outlined in the Supporting Information.

Table 3. 1. Details of the nanoparticle-loaded polyimide (PI) systems

Nanoparticle	Nanoparticle Concentration (wt%)	Designation	Number of Molecules (PI/Nanoparticle)	Simulation Cell Size ($Å^3$)
None	0	Neat PI	240/0	43×43×55
Pristine POSS	15	PI-pPOSS-15	240/30	44×44×53
	30	PI-pPOSS-30	240/80	44×44×52
PI-grafted POSS	15	PI-gPOSS-15	210/30	44×44×53
	30	PI-gPOSS-30	160/80	44×44×52
Randomly Oriented Gr	15	PI-Gr-Random-15	240/4	46×46×47
Aligned Gr	15	PI-Gr-Aligned-15	236/4	46×46×48
Randomly Oriented CNT	15	PI-CNT-Random-15	240/4	46×46×48
Aligned CNT	15	PI-CNT-Aligned-15	230/4	46×46×49

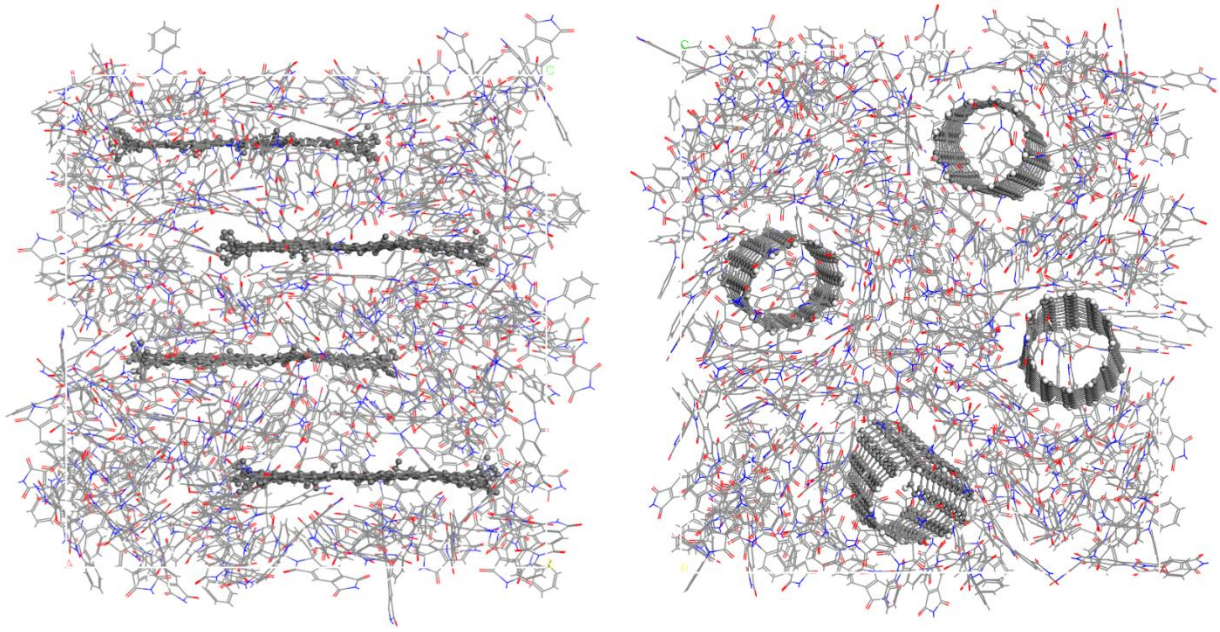

Figure 3. 1. Representative initial snapshots of the energy-minimized PI systems loaded with (a) aligned Gr and (b) aligned CNT nanoparticles.

Once equilibrated, the final atomic coordinates of the systems were exported to the LAMMPS software package[25] into a 2D-periodic simulation cell with periodicity in the *x* and *y* directions. A vacuum slab was placed on top of the systems in the *z* direction. Next an NVE (constant number of atoms, N; constant volume, V; constant energy, E) simulation was run for each system for a total of 10 ps using the reactive force field (ReaxFF)[28, 65] until the system temperatures were stabilized at 298 K. It is noteworthy to mention that ReaxFF has been used in the past for the reactive simulation of the various components in our nanoparticle-loaded PI systems, i.e., PI,[63] POSS,[63] CNT,[66] and Gr.[62] Therefore, ReaxFF is deemed to be a suitable force field for the simulation of material systems in this work. The ReaxFF parameters for silicon were taken from the work of van Duin et al.[67] and those for carbon, hydrogen, oxygen, and nitrogen were taken from the work of Chenoweth et al.[28] The complete set of the ReaxFF parameters used in this work is given in the Appendix B. In these simulations, the time step and cut-off distance were set

at 0.1 fs and 9 Å, respectively. Then another NVE simulation was run for a total simulation time of 35 ps, during which the material surface was bombarded with oxygen atoms in 200 fs intervals from a distance of 70 Å above the material surface and with the velocity of 0.074 Å/fs (= 7.4 km/s)[63] in the *z* direction. This velocity of the AO species was fixed in this work to match the real AO bombardment event. However, the variability in the position of the AO bombardment in the defined region above the surface of the different material systems is taken into account when repeating the simulations, since the algorithm performs the bombardment randomly in the defined region. The trajectory files were saved every 200 fs and analyzed to generate mass loss data, mass density profiles, damage propagation depths, AO penetration depths, erosion yields, and temperature evolution profiles for the different systems.

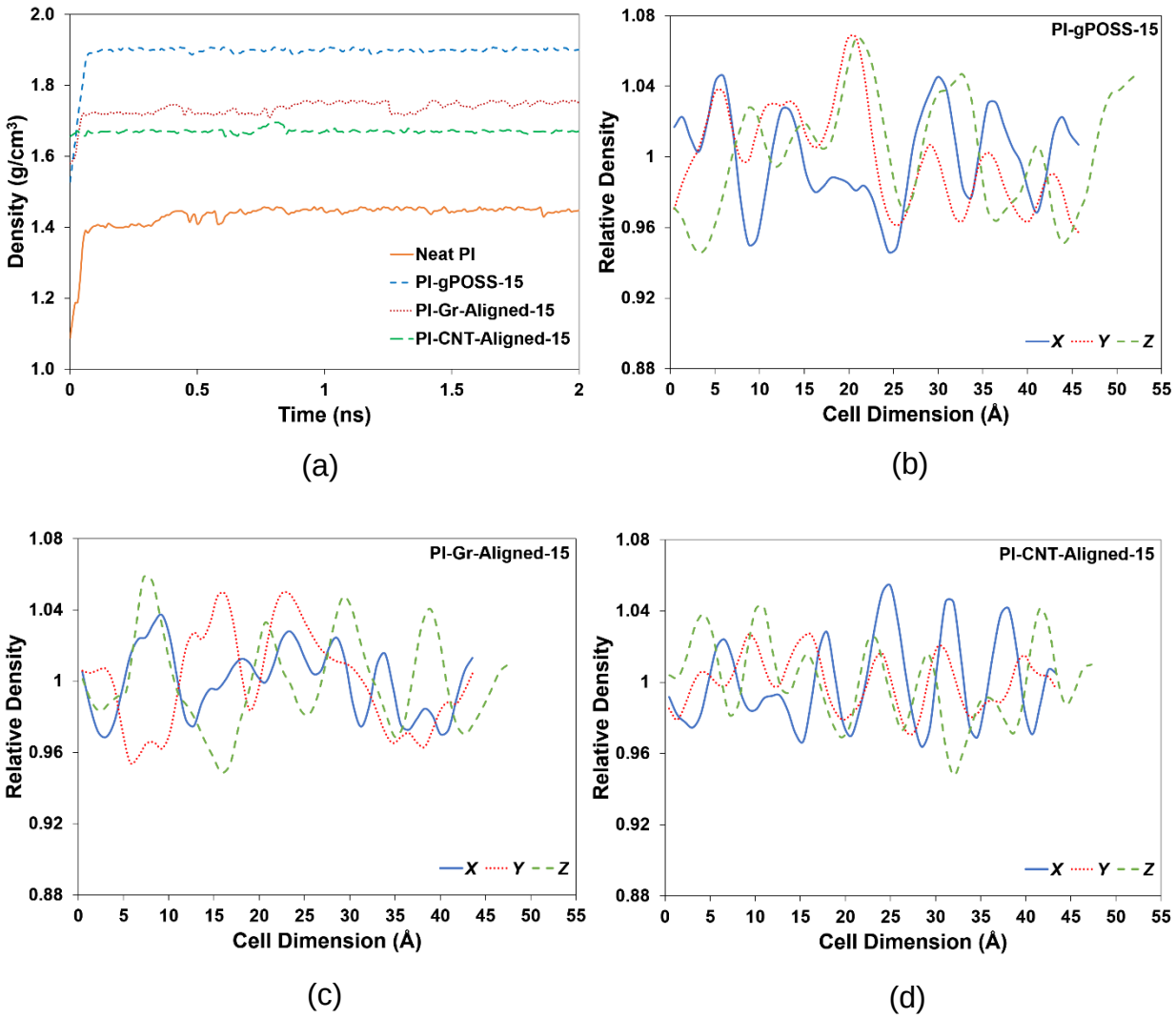

Figure 3. 2. (a) Representative density evolution profiles for select systems during the equilibration of initial structures; (b)-(d) relative density (ρ/ρ_{bulk}) distribution in the simulation cells for representative systems after 2 ns of equilibration.

3.4. Results and Discussion

Representative initial (t = 0 ps) and final (t = 35 ps, equivalent to a fluence of 10^{15} O atoms/cm^2) snapshots of all nanoparticle-loaded PI systems (Table 3.1) are shown in Figure 3.3. The neat PI system undergoes a relatively rapid damage when exposed to the hypervelocity AO species (Table 3.1), consistent with the observations of Rahnamoun and van Duin.[63] In what follows, the data

for the Neat PI system are used as control when comparing between the nanoparticle-loaded PI systems. Moreover, the behavior of the PI-POSS systems will be elucidated first to reveal the effects of POSS grafting and concentration on the resistance of the material to the AO bombardment damage. Next, we compare the damage mitigating effects of the different nanoparticles (POSS, Gr, and CNT) and alignment in Gr and CNT on the nanoparticle-loaded PI systems.

Averaged normalized mass loss as a function of simulation time and fluence is given for the PI-POSS systems in Figure 3.4a. Mass loss for each system is normalized at each time step with respect to the respective total mass of the initial system. In Figure 3.4a, the data are compared for the pristine and grafted POSS systems at the low and high POSS concentrations (15 wt% and 30 wt%, respectively) versus that of the Neat PI system. As seen in this figure, the Neat PI system undergoes a rapid degradation as opposed to those of the POSS-loaded PI systems. The onset of material degradation (mass loss) occurs at lower AO exposure times for the PI-pPOSS-15 system (about 7 ps, equivalent to a fluence of 1.85×10^{14} O atoms/cm^2 or bombardment with 35 AO species) than that of the PI-gPOSS-15 system (about 13 ps, equivalent to a fluence of 3.40×10^{14} O atoms/cm^2 or bombardment with 65 AO species). This observation indicates that grafting of the POSS nanoparticles with PI molecules improves the AO damage mitigation efficacy in the PI-POSS systems (see also Figures 3a and 3b). When nanoparticles are grafted with the resin molecules, their dispersion is improved in the resin.[68] In other words, the nanoparticles are better stabilized in the resin, leading to a reduced agglomerated state. The occurrence of this phenomenon is confirmed in Figure 3.4b, where the radial distribution functions (RDFs) of the Si-Si atomic pairs in the pPOSS- and gPOSS-loaded PI systems are compared at the same concentration (15 wt%). The overlapping peaks at about 2.5 Å are associated with the Si-Si atomic distances within

the same POSS structure. The peaks at about 1.5 Å for pPOSS and 3 Å for gPOSS are associated with the Si-Si atomic distances in different POSS nanoparticles. These results indicate that the POSS nanoparticles are closer to one another in the pPOSS system, signifying a more agglomerated state when compared to the gPOSS system.

An increase in the POSS nanoparticle concentration leads to an increase in the damage mitigation efficacy of both pPOSS- and gPOSS-loaded PI systems (Figure 3.4a). Since POSS nanoparticles are highly resistant to damage by AO bombardment,[63] an increase in their concentration is expected to improve the damage mitigation efficacy of the PI-POSS systems. All in all, the grafting of POSS with PI has a more pronounced damage mitigation effect against AO bombardment. This point will be revisited later when the erosion yield data are compared for the different systems.

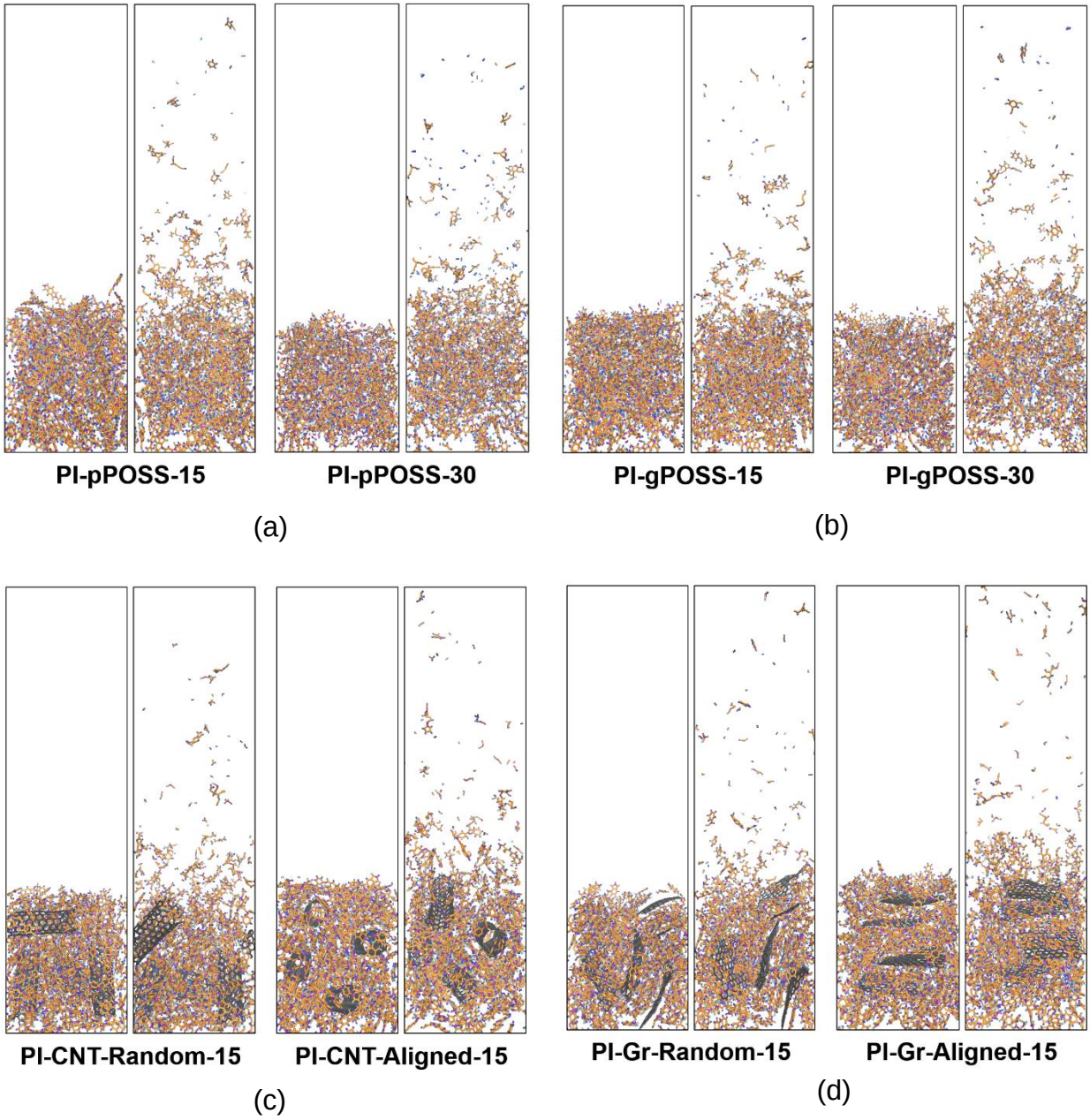

*Figure 3. 3. Representative initial (*t = 0 ps) *and final (*t = 35 ps) *snapshots of the PI systems loaded with (a) pristine POSS (left: 15 wt% and right: 30 wt%), (b) PI-grafted POSS (left: 15 wt% and right: 30 wt%), (c) CNT (left: randomly oriented and right: aligned), and (d) Gr (left: randomly oriented and right: aligned). The details of the systems are given in Table 3.1. 35 ps of simulation is equivalent to a fluence of* 10^{15} *O atoms/cm*^{2}.

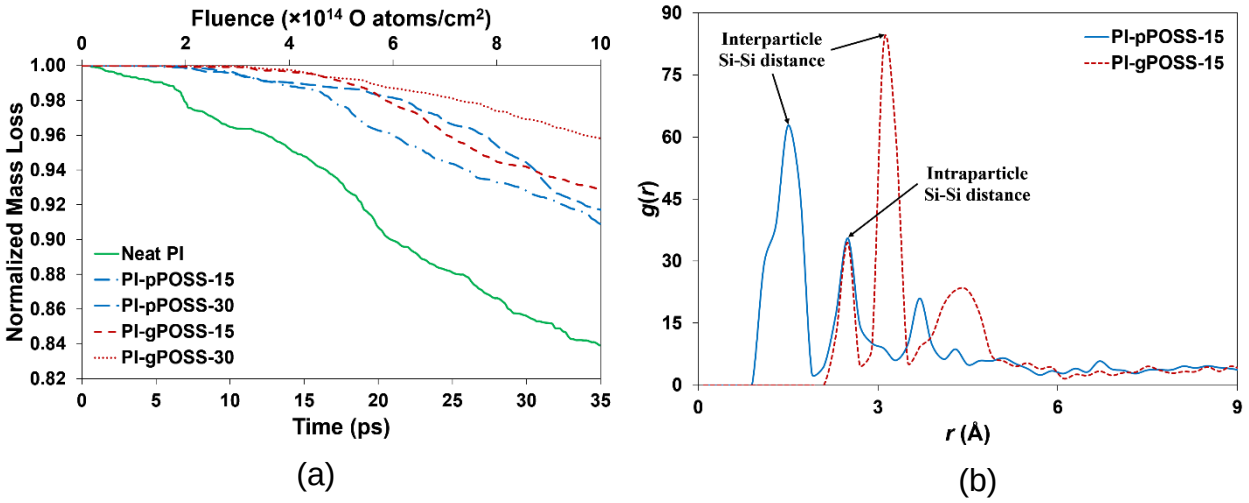

Figure 3. 4. (a) Averaged normalized mass loss as a function of simulation time and fluence for the neat polyimide (PI) and loaded-PI systems with pristine and grafted POSS nanoparticles (pPOSS and gPOSS, respectively) at two nanoparticle concentrations of 15 wt% and 30 wt%; (b) radial distribution function showing the Si-Si intraparticle and interparticle atomic distances in the different PI-POSS systems.

In Figure 3.5, averaged normalized mass loss of the PI-gPOSS system is compared to those of the PI systems loaded with randomly oriented and aligned Gr and CNT nanoparticles. The nanoparticle weight fraction is fixed at the lower 15 wt% concentration for a valid comparison between the systems. As seen in this figure, the PI system loaded with randomly oriented CNTs or Gr nanoparticles exhibit a higher resistance to the AO bombardment damage than the other systems, as evidenced by their late onset of mass loss (about 24 ps, equivalent to a fluence of 6.25×10^{14} O atoms/cm^2 or bombardment with 120 AO species). In contrast, the PI systems loaded with aligned CNT and Gr nanoparticles have the lowest damage (onset of mass loss for both systems at about 10 ps, equivalent to a fluence of 2.63×10^{14} O atoms/cm^2 or bombardment with 50 AO species).

Erosion yield, defined as the average mass loss divided by the number of oxygen atoms that have impacted the material,[69] is listed for the different systems at different AO exposure times in Table 3.2. As it is customary in MD simulation, the erosion yield data are reported in terms of g/AO rather than cm^3/AO.[46, 63] This is mainly due to the difficulty in measuring the volume of disintegrated species. When comparing the chemical species evolved during material degradation, smaller molecules, such as H_2, O_2, HO, H_2O, CO, and CO_2, are among the first to appear in all systems at lower erosion yield values, followed by longer chain hydrocarbon-based species, such as C_6H_3O, C_6H_4, C_6H_4O, and C_6H_5, at higher erosion yield values. As mentioned previously, grafting of the POSS nanoparticles has a larger effect on the damage mitigation efficacy of the POSS-loaded PI systems than POSS concentration. When comparing between all POSS-loaded PI systems, the former generally lowers the erosion yield by a factor of about 4, while the latter lowers it by a factor of about 1.5 (Table 3.2). Consistent with the mass loss data (Figure 3.5), the PI systems with randomly oriented Gr and CNT nanoparticles, which show significantly lower erosion yield values at different AO exposure times (Table 3.2, underlined systems), give higher damage mitigation efficacy than the other systems. During our simulations, the PI was the only component that underwent degradation when exposed to the AO attack. Atar et al.[51] report a similar observation for the early degradation of PI, as opposed to CNT and POSS, in PI/CNT and PI/CNT-POSS systems. Since Gr and CNT have a similar carbon-based structure to that of PI, their degradation is expected to be on equal footing with that of PI. However, this is not the case and PI undergoes a faster degradation, which is attributed to its higher erosion yield.[38, 51, 70] To further investigate why the carbon-based nanoparticles (CNT and Gr) can mitigate the AO damage in CNT- and Gr-loaded PI systems, a system composed of 13 relaxed layers of hydrogen-terminated pristine Gr sheets (46×46 $Å^2$) were subjected to AO bombardment under the same

conditions as the those of the nanoparticle-loaded PI systems. The schematics of the layered Gr system, AO penetration depth, and normalized mass loss are shown in Figure 3.6.

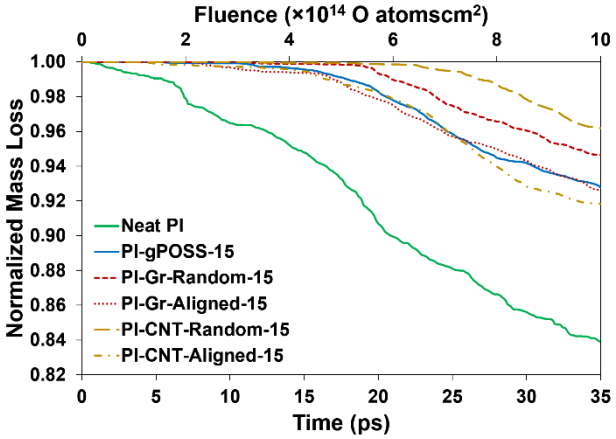

Figure 3. 5. Averaged normalized mass loss as a function of simulation time and fluence for the neat polyimide (PI) and loaded-PI systems with grafted POSS (gPOSS), as well as randomly oriented and aligned Gr and CNT nanoparticles, at a concentration of 15 wt%.

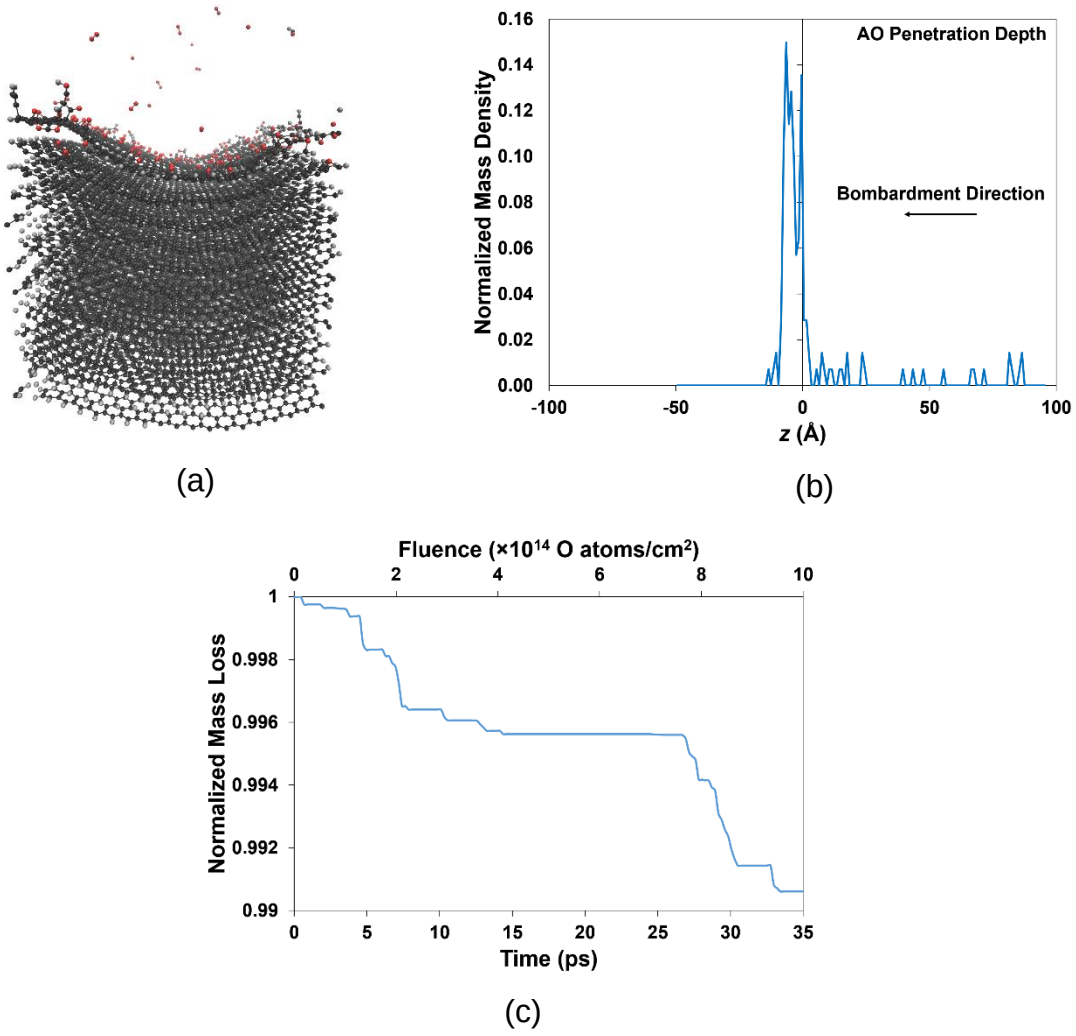

Figure 3. 6. (a) Final snapshot of a layered hydrogen-terminated Gr system (black = carbon, silver = hydrogen) bombarded with atomic oxygen (AO) species (red), (b) final normalized mass density profile of the AO (material surface is located at z = 0 Å) in the layered Gr system, and (c) normalized mass loss as a function of simulation time and fluence for the layered Gr system bombarded with AO.

Almost all AO species react with the topmost Gr layer and are prevented from penetrating the system as evident in Figures 6a and 6b. Moreover, there is an insignificant mass loss observed for the layered Gr system during the simulation, which indicates that the Gr sheet retains its integrity during AO bombardment. Therefore, it is deduced that the Gr nanoparticles can indeed

protect the PI by reacting with the AO species and preventing them from decomposing the PI molecules. The same can hold true for the CNT particles.

Experimental observations indicate that the erosion yield of the PI/POSS system (at a POSS concentration of 8 wt%) is reduced by a factor of about 4 compared to that of the neat PI.[40] However, the erosion yield of PI/CNT system is reduced by only a factor of 1.25.[40] Moreover, to the best of our knowledge, there are no experimental erosion yield reports for the PI/Gr system. The erosion yield data obtained in this work for PI/g-POSS, PI/CNT-Aligned, and PI-Gr-Aligned (Table 3.2) match the above experimental trends. Both Novikov et al.[40] and Atar et al.[51] report a more exposed surface for the PI in the PI/CNT system compared to that of PI/POSS during the early period of the system degradation. Therefore, the PI/CNT system exhibits a higher erosion yield than that of PI/POSS. In our simulations, the PI/CNT-Aligned and PI-Gr-Aligned systems have more exposed surface for the PI (60 PI molecules for the PI/CNT-Aligned and 50 PI molecules for the PI-Gr-Aligned system) than that of the PI/gPOSS-30 system (45 PI molecules); therefore, they exhibit a higher erosion yield consistent with the experimental observations. On the other hand, the PI/Gr-Random (42 PI molecules) and PI-CNT-Random (40 PI molecules) systems have less exposed PI than that of the PI-gPOSS-30 system, leading to lower erosion yield values for the former systems. The exposed PI molecules for the different systems were calculated for a 15-Å deep region from the exposed surfaces of the material systems before the initiation of the AO bombardment. It has to be mentioned that all the above observations are valid for the early stage of degradation, when the nanoparticles themselves have not undergone degradation. POSS is reportedly more resistant to the AO attack damage than Gr or CNT.[51] Randomly oriented CNTs and Gr nanoparticle are “well-dispersed” in our systems on the individual nanoparticle level. This level of dispersion is very difficult, if not impossible, to obtain in practice. Therefore, in the

experimental data for the PI/CNT systems, CNTs are expected to be in a more agglomerated state.[40, 51]

Table 3. 2. Average erosion yield[69] at different atomic oxygen exposure times

System \ n_{AO} [a] →	Erosion Yield ($\times 10^{-24}$ g/O atom)				
	13	21	41	72	89
Neat PI	4.20	18.32	44.20	79.93	89.90
PI-pPOSS-15	0.00	2.15	5.25	25.00	37.50
PI-pPOSS-30	0.06	0.10	2.02	28.50	29.00
PI-gPOSS-15	0.00	0.72	1.52	5.70	11.60
PI-gPOSS-30	0.00	0.45	0.43	0.31	7.55
PI-Gr-Random-15	0.00	0.00	0.06	1.33	1.79
PI-Gr-Aligned-15	0.00	0.57	1.83	11.10	16.75
PI-CNT-Random-15	0.00	0.00	0.25	0.68	0.56
PI-CNT-Aligned-15	0.06	2.55	7.95	9.55	21.50

[a] Number of atomic oxygen species that have impacted the material systems

Note: The underlined systems have lower erosion yield.

To better elucidate the extent of damage in all nanoparticle-loaded PI systems exposed to hypervelocity AO species, an average damage propagation depth (DPD) (Figure 2.7 and Table 3.3) and an average AO penetration depth (Figure 3.8) were calculated in this work. DPD was determined based on a comparison between the normalized mass density profiles for the initial and final configurations of the systems along the *z*-axis (parallel to the AO bombardment direction). Accordingly, the approximate distance between the point within the material corresponding to the onset of drop in the normalized mass density and the system surface is given as a measure of DPD.

The AO penetration depth (Figure 3.8) is calculated from the profile of the normalized AO mass density in the simulation cell (along the *z*-axis) averaged over the last 2,000 steps of the simulation.

As seen in Figure 3.7, which gives an example of the normalized mass density profile for the PI-Gr-Aligned-15 system, damage extends to a depth of about 15 Å. The DPD data for the other systems are given in Table 3.3, where the DPD shows a decreasing trend with an increase in the POSS concentration in the PI-POSS systems and with grafting of the POSS nanoparticles (compare to Figures 3a and 3b). Moreover, the alignment of nanoparticles in the PI-Gr and PI-CNT systems does not affect the DPD appreciably (Table 3.3). When comparing the PI-gPOSS with PI-Gr and PI-CNT systems, they all give similar DPD values. The same observation is made for the AO penetration depth data in Figure 3.8, which indicate that the AO penetration depths in the PI-gPOSS systems are, in general, similar to those of the PI-Gr and PI-CNT systems. These observations are, in general, consistent with those of the normalized mass loss data in Figures 4 and 5.

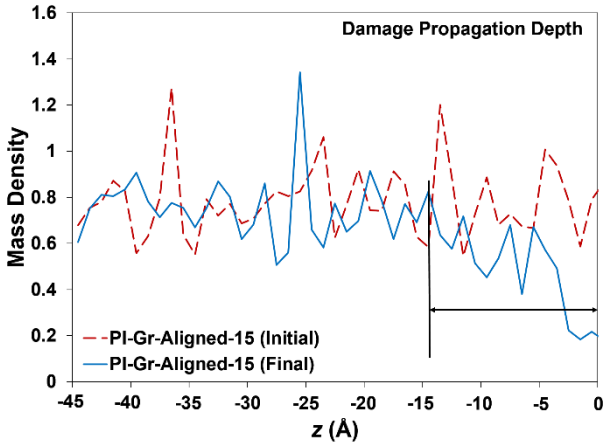

Figure 3. 7. An example of the final normalized mass density profiles along the z-axis of the PI systems loaded with aligned graphene nanoparticles. The material surface is located at z = 0 Å. The damage propagation depth is shown by the arrow.

Table 3. 3. Average damage propagation depth (DPD) for different nanoparticle-loaded polyimide (PI) systems bombarded with AO species

	Neat PI	POSS				Gr		CNT	
		Pristine		PI-Grafted					
		15 wt%	30 wt%	15 wt%	30 wt%	Random	Aligned	Random	Aligned
DPD (Å)	28.5	25.5	21.8	20.3	15.3	15.3	15.1	18.3	18.8
St. Dev.[a] (Å)	1.1	0.4	0.2	0.2	0.2	0.4	0.2	0.4	0.6

[a] Standard deviation

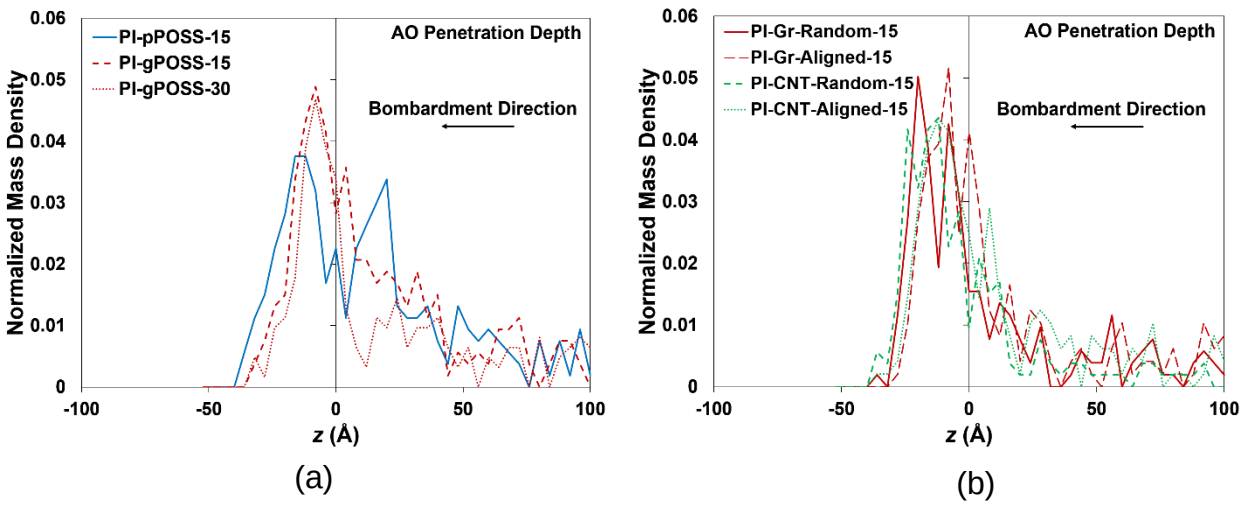

Figure 3. 8. Representative final normalized mass density profiles of the atomic oxygen (AO) in (a) PI-POSS and (b) PI-Gr and PI-CNT systems. The material surface is located at z = 0 Å.

Representative temperature evolution profiles for the PI-POSS-15, PI-Gr-15, and PI-CNT-15 systems are given in Figure 3.9. As seen in this figure, the PI-Gr-15 and PI-CNT-15 systems (randomly oriented or aligned) exhibit lower temperature rise upon AO bombardment than those of the PI-POSS-15 systems. This is a desirable behavior, consistent with the observations for mass loss (Figure 3.5), DPD (Table 3.3), and AO penetration depth (Figure 3.8). However, it is difficult to suggest a correlation between temperature evolution and mass loss or DPD.

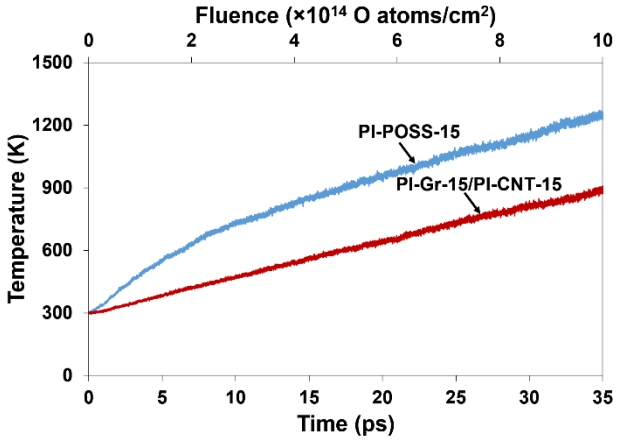

Figure 3. 9. Representative temperature evolution profiles for the PI-POSS-15, PI-Gr-15, and PI-CNT-15 systems. The profiles for the PI systems loaded with pristine or PI-grafted POSS, as well randomly oriented or aligned Gr or CNT systems are very similar.

3.5. Conclusion

Atomic oxygen (AO) bombardment of spacecraft in the low Earth orbit poses a great hazard to their durability and safe operation in near-Erath and space missions. Through a concerted research effort in recent years, nanoparticle-enhanced polymer matrices have been shown to possess promising AO damage mitigation and erosion-inhibiting characteristics when used as a top coating on the spacecraft body structures. However, due to the presence of a variety of lower length scale phenomena associated with nanoparticle/polymer systems and their behavior toward AO attack, a fundamental understanding of key interactions between nanoparticle type, morphology, level of dispersion, concentration, and surface chemistry is warranted. This objective is fulfilled in this work by considering three classes of nanoparticles, i.e., polyoctahedral silsesquioxane (POSS), graphene (Gr), and carbon nanotubes (CNTs). The main research focus in recent years on the AO bombardment damage mitigation has been on the use of POSS nanoparticles and considerably less

attention has been given to CNT and almost no attention to Gr. For the latter two, orientation of nanoparticles may also play a role in their damage mitigation capability.

In this work, the effect of surface modification of POSS and its concentration in a polyimide (PI) matrix, as well as the effect of nanoparticle type (POSS, Gr, and CNT) and the nanoparticle orientation in Gr and CNT nanoparticles in the PI matrix were studied using a reactive molecular dynamics simulation methodology. Among all systems, PI with randomly oriented CNTs or Gr nanoparticles gave, in general, the lowest mass loss, erosion yield, surface damage, AO penetration depth, and temperature. These observations are attributed to the lowest amount of exposed PI at the material surface in agreement with the experimental findings for the early degradation period (before the onset of nanoparticle degradation). It should be mentioned here that POSS is more resistant to the AO attack damage than Gr or CNT. It is practically impossible to prepare PI-CNT or PI-Gr systems with well-dispersed CNTs or Gr nanoparticles on the individual level. However, our results indirectly show the significant effect of CNT or Gr dispersion in the PI matrix on the AO damage mitigation. The PI-CNT and PI-Gr systems also show a slower temperature rise than those of the PI-POSS systems, which is a desirable material behavior.

Grafting of the POSS nanoparticles with PI and the increasing the PI concentration lowers the erosion yield of the PI-POSS systems, with the effect of former being greater on the AO damage mitigation. When grafted, the POSS nanoparticles give better dispersion in the PI matrix, thereby reducing the amount of exposed PI on the material surface. Therefore, their AO damage mitigation efficacy becomes almost on par with the PI systems with randomly oriented CNTs or Gr nanoparticles. The results of this fundamental study shed light on the lower length scale phenomena associated with AO damage mitigation in different PI-nanoparticle systems.

3.6. Acknowledgment

The authors wish to acknowledge Jason G. Hale, Director of the Office of Research and Sponsored Programs at the University of Mississippi, and Alexander H. D. Cheng, Dean of the School of Engineering at the University of Mississippi, for their support of this work.

CHAPTER IV

Thermal Analysis of Montmorillonite/Graphene Double-layer Coating as a Candidate Lightning Strike Protective Layer for Crosslinked Epoxy by Molecular Dynamics

In this chapter, the through-thickness temperature distribution and thermal conductivities of unprotected neat crosslinked epoxy, and protected epoxy/Gr, and epoxy/MMT/Gr systems against lightning strike damage was investigated.

4.1. Abstract

Molecular dynamics simulations were performed to determine thermal conductivities and through-thickness temperature profiles of unprotected crosslinked epoxy, as well as protected epoxy with graphene (Gr) and montmorillonite (MMT)/Gr surface coatings against lightning strike damage. Three hot surface temperatures of 500 K, 1,000 K, and 10,000 K, corresponding to the initial stages of the temperature rise at the lightning strike site, were used, while the cold surface was kept at 298 K. The MMT/Gr double-layer coating provided the most efficient thermal shielding of the epoxy sublayer, even at 10,000 K. Much less efficient thermal shielding was observed for the Gr coating.

4.2. Introduction

Lightning strike damage protection is a critical aspect of the design of modern aircraft composite structures. Near the lightning strike site on a composite part, a peak current of about 200 kA and a

maximum temperature of about 20,000°C may be observed in a fraction of a second.[71] As composite materials gradually replace aluminum in critical aircraft parts, such as fuselage and wings, the lightning strike hazard increases to alarming levels because of a generally lower electrical and thermal conductivities of the composite materials compared to aluminum. Therefore, it is imperative to protect the new-generation composite-heavy aircraft, such as Boeing 787 Dreamliner, against catastrophic failure due to lightning strike damage. During the strike event, the polymer matrix, which is generally epoxy, decomposes through ignition and pyrolysis followed by a catastrophic fiber delamination in the composite. To mitigate the localized damage, the electric charge needs to be swiftly distributed over a large surface area. Moreover, the transverse heat conduction should be minimized by employing a suitable thermal shielding mechanism. While the use of metal meshes and ply-integrated interwoven wires[72] have proven to be effective in the lightning strike protection of fiber-reinforced composites, these meshes and wires significantly increase the weight of the structures. Herein, the efficacy of a novel lightweight montmorillonite (MMT)/graphene (Gr) double-layer protective top coating in mitigating the lightning strike damage extent in the crosslinked epoxy sublayer is investigated using molecular dynamics (MD) simulation. Gr is known to possess excellent electrical and thermal conductivities,[73] while montmorillonite is known for its superior thermal shielding characteristics.[74] Though lightning is an electrothermal phenomenon, the current work only focuses on the thermal degradation aspects of the strike event, thereby providing molecular insights into the thermal shielding behavior of the MMT/Gr coating. While the thermal properties of Gr[75] and Graphene oxide,[76] Gr/epoxy[77] and MMT/epoxy[78] systems have been studied before, to the best of our knowledge, the thermal behavior of an epoxy/MMT/Gr multilayer system

has not been investigated yet. In what follows, the MD simulation details and thermal analysis data are presented.

4.3. Computational Details

All initial chemical structures were created in BIOVIA Materials Studio (V8.0). Initially, 207 epoxy monomers (Bisphenol A diglycidyl ether (DGEBA) with chemical formula $C_{21}H_{24}O_4$) were randomly packed with 207 curing agent molecules (1,3-phenylenediamine) at 298 K in a 3D-periodic simulation box (size: 40×40×100 $Å^3$, target density: 1.2 g/cm^3) in the Amorphous Cell module of Materials Studio. All simulations in the work were performed using the Consistent Valence Forcefield (CVFF).[79] This forcefield has previously been used for the MD simulation of similar systems, such as Gr-polymer[80] and polymer-MMT[81] and is deemed appropriate for this work. Next, a geometry minimization was performed on the epoxy/curing agent system using the Conjugate Gradient method[82] followed by equilibration of the system at 298 K using the NPT ensemble for 1 ns. In all simulations, a time step of 1 fs was used. The cut-off distance for long-range intermolecular interactions was fixed at 12 Å. The system temperature and pressure were controlled by Andersen thermostat and barostat,[83] respectively. Once the system density was equilibrated at around 1.18 g/cm^3, a crosslinking algorithm in Materials Studio was employed with an initial target of 100% curing agent conversion. After the conclusion of the crosslinking procedure, an actual conversion of 90% was achieved for the curing agent.

Next, MMT crystal structure (a = 5.171 Å, b = 8.956 Å, and c = 9.740 Å; α = 90º, β = 96.1º, γ = 90º)[84] was imported from the American Mineralogist Crystal Structure Database (Figure 1). Three stacked MMT layers were constructed from this unit crystal in the size of 40×40×27 Å. Finally, six layers of pristine graphene (Gr) (size: 40×40 $Å^2$) were separately stacked at an equilibrium interlayer distance of 4 Å. In this work, the number of Gr and MMT layers were fixed

at six and three, respectively, and the effects of the number of Gr and MMT layers on the thermal properties of the composite systems were not investigated. Altogether, three systems were constructed from the above base layers in Materials Studio: 1) neat crosslinked epoxy, 2) crosslinked epoxy/Gr, and 3) crosslinked epoxy/MMT/Gr (Figure 4.1). Next, these systems were imported to the LAMMPS software package and equilibrated at 298 K using the NPT ensemble for 10 ns. Then, a 2D simulation was run (periodicity in the *x* and *y*-directions) on the equilibrated structures using the NVE ensemble for 1 ns, where the top surface was subjected to temperatures of 500 K, 1,000 K, and 10,000 K (hot surface in Figure 4.1) and the bottom surface was kept at 298 K (cold surface in Figure 1). Once the systems reached thermal equilibrium, a through-thickness temperature profile was generated for each case. An example of temperature profile evolution with increasing simulation time is given for the neat crosslinked epoxy system in Figure 2. In this figure, the temperature profiles at 5 ns and 10 ns overlap, signifying the achievement of thermal equilibrium. Also, Müller-Plathe's algorithm[85] was employed to calculate the thermal conductivity of various systems. For this purpose, a 3D-periodic simulation box of each system was divided into *N* slabs (1 Å thick) perpendicular to the *z*-direction. Thermal conductivity was then calculated using the following formula:[85]

$$\lambda = \frac{\sum_{transfers} \frac{m}{2}\left(v_h^2 - v_c^2\right)}{2tL_xL_y\left\langle \frac{\partial T}{\partial z} \right\rangle}, \tag{4.1}$$

where t is the simulation time, m is the particle mass, L_x and L_y are the simulation box lengths in *x*- and *y*-directions, respectively, T is the temperature, and v is the atomic velocity. Subscripts h and c refer to *hot* and *cold* atom, respectively. The sum is over all kinetic energy transfers between

the particles and the temperature gradient in the *z*-direction is ensemble-averaged. More details about the algorithm are given in Müller-Plathe's work.[85]

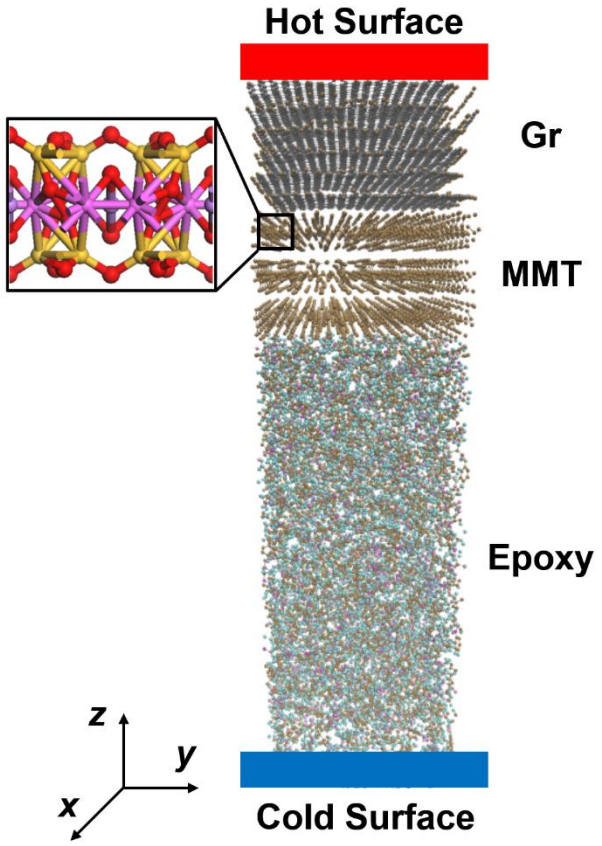

Figure 4. 1. Initial snapshot of the epoxy/MMT/Gr triple-layer system. The unit crystal structure of MMT is shown in the zoomed-in view.

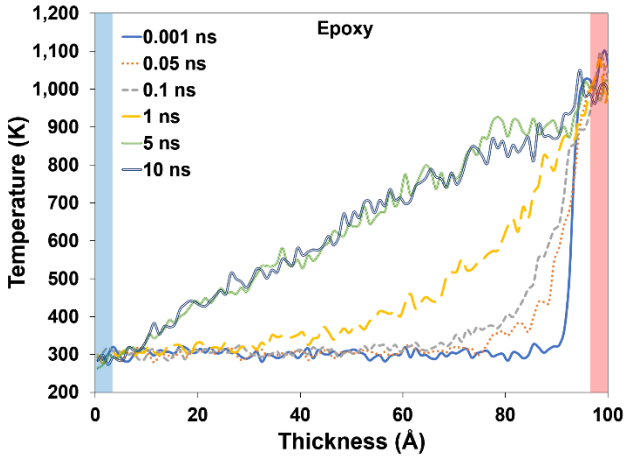

Figure 4. 2. Evolution of through-thickness temperature profile in the neat crosslinked epoxy system with increasing simulation time.

4.4. Results and Discussion

The equilibrium temperature distribution along the *z*-axis (Figure 4.1) are given for the two protected epoxy systems, i.e., epoxy/Gr and epoxy/MMT/Gr, as well as the control epoxy system for each of the three surface temperatures (500 K, 1,000 K, and 10,000 K) in Figure 4.3. The unprotected epoxy system shows a near-linear temperature profile, wherein the local temperature decreases from the hot to cold surface for all three cases of surface temperatures. At 1,000 K (Figure 4.3a) and 10,000 K (Figure 4.3b), about 50% and 95% of the epoxy is expected to undergo thermal degradation, respectively. This indirect prediction is based on the crossing of the local temperature over the line marking the thermal degradation onset temperature for the neat crosslinked epoxy (680 K). It should be mentioned herein that the thermal degradation of epoxy is only inferred from the thermal distribution in this work. This analysis is just suggestive and not based on the actual complex physics and chemistry of thermal degradation that may be responsible for the degradation phenomenon.

When a Gr protective layer is applied to the surface of epoxy (epoxy/Gr system), a moderate drop is observed for the maximum epoxy surface temperature, as well as the slope of the linear

profile (Figure 4.3). In addition, a decrease in the local temperature is observed when transitioning between the Gr sheets in the protective Gr layer, which is most noticeable for the first-to-second Gr sheet transition at 500 K (Figure 4.3a). This phenomenon is attributed to the lower transverse thermal conductivity of Gr compared to its longitudinal thermal conductivity. At the epoxy/Gr interface, another drop in the local temperature is observed, which is most noticeable at 10,000 K (Figure 4.3c). This phenomenon is due to a strong phonon scattering at the epoxy/Gr interface as a result of a weak bonding and phonon mismatch between the epoxy and Gr layers. The data in Figure 4.3 indicate a relatively moderate thermal protection is observed when coating the crosslinked epoxy with Gr. The thermal protection efficacy of the Gr layer is more pronounced at lower surface temperatures (about 25% of epoxy is expected to undergo thermal degradation at 1,000 K) (Figure 4.3b) and is deteriorated at 10,000 K (Figure 4.3c).

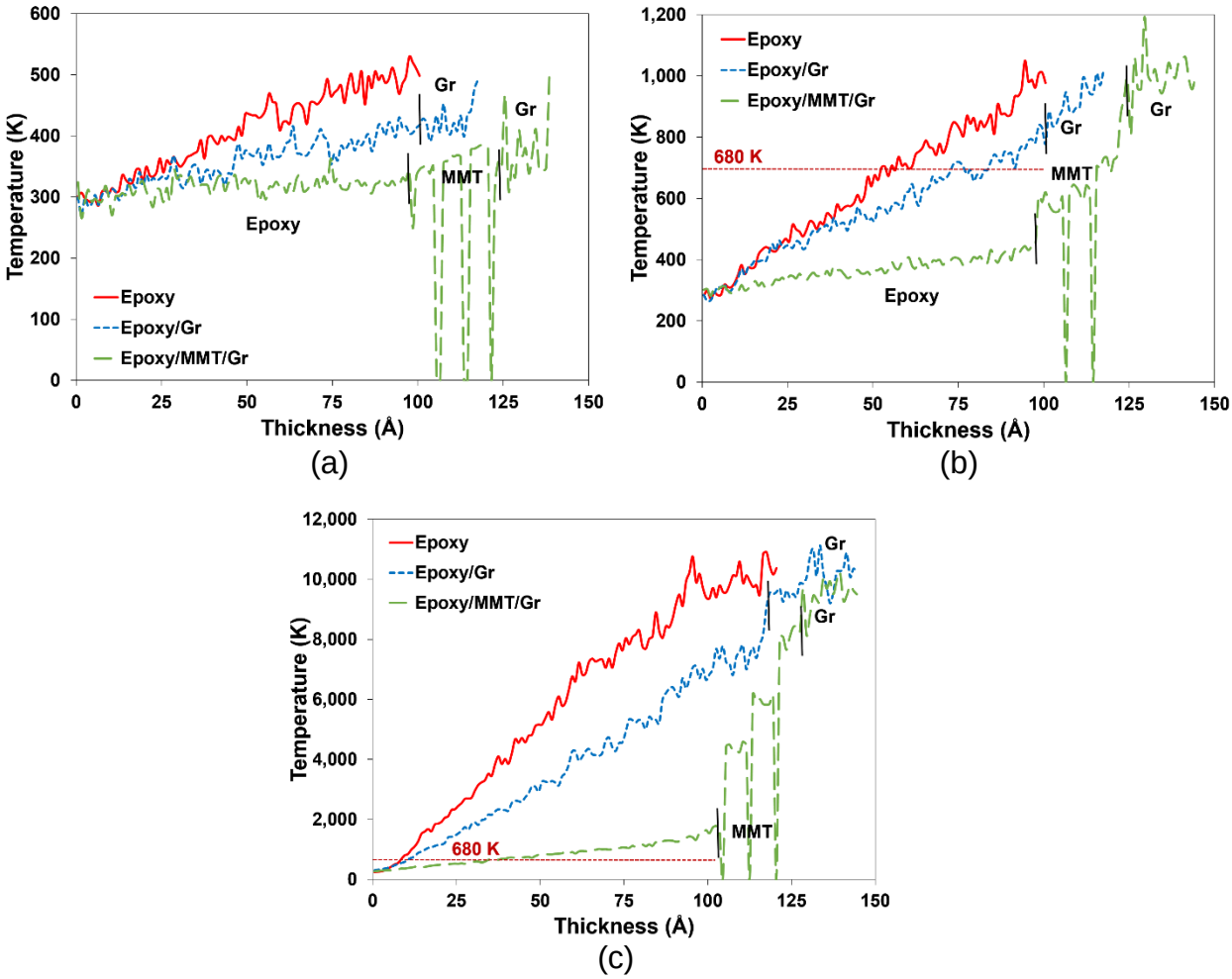

Figure 4. 3. Through-thickness equilibrium temperature profiles in the epoxy, epoxy/Gr, and epoxy/MMT/Gr systems when the hot surface is at (a) 500 K, (b) 1,000 K, and (c) 10,000 K. The cold surface is kept at room temperature (298 K).

The most significant thermal protection is observed when a MMT/Gr double-layer coating is applied to the epoxy surface (epoxy/MMT/Gr system). Interestingly, only about 50% of epoxy is expected to undergo thermal degradation at 10,000 K (Figure 4.3c) with essentially no degradation at the lower surface temperature of 1,000 K (Figure 4.3b). In this case, the thermal barrier effect of MMT is very noticeable at all low, moderate, and high temperatures. Generally, transitioning between each MMT layer, a sharp drop of local temperature to essentially 0 K is observed, which

is attributed to the existence of local vacuum in the interlayer spacing. This successive layer-by-layer thermal shielding is clearly seen in Figure 4.3.

Thermal conductivities (λ) of the neat crosslinked epoxy, epoxy/Gr, and epoxy/MMT/Gr systems are given in Table 1. By applying a top Gr coating to the neat crosslinked epoxy, a 26% reduction in the thermal conductivity of the composite is observed. However, a top coating of MMT/Gr brings about a nearly 100% reduction in the thermal conductivity of the system. This signifies a nearly total thermal shielding of the epoxy sublayer when the MMT/Gr system is used as the top coating.

Table 4. 1. Thermal conductivities (λ) of the various systems

System	λ ($W/m^2 K$)	Experimental λ ($W/m^2 K$)
Epoxy	0.12±0.07	0.15-0.25[a]
Epoxy/Gr	0.09±0.07	-
Epoxy/MMT/Gr	0.0001±0.00003	-

[a] From the work of Chung and Lin[24]

4.5. Conclusions

In summary, by computationally investigating the through-thickness temperature distribution and thermal conductivities of unprotected neat crosslinked epoxy, and protected epoxy/Gr, and epoxy/MMT/Gr systems against lightning strike damage, it is inferred that the MMT/Gr top coating has great potential to be used as a lightning strike damage protection measure for epoxy-based composite systems. A more thorough multi-physics (electrothermal) analysis of the epoxy/MMT/Gr system may further reveal its lightning strike damage mitigation efficacy.

4.6. Acknowledgements

This work was sponsored by a re-grant from the National Aeronautics and Space Administration (NASA) through the Mississippi Space Consortium under the grant number NNX15AH78H. The authors also wish to acknowledge Dr. Nathan E. Murray for his support.

CHAPTER V

CONCLUSIONS

Molecular dynamics simulation is an invaluable tool to probe the lower length and time scale phenomena associated with the physico-chemo-mechanical changes of the material in response to external extreme and catastrophic conditions. In this dissertation, both reactive and non-reactive molecular dynamics simulation were employed to elucidate the lower length scale phenomena associated with the response of hybrid materials to three harsh and extreme environments.

In the first part of dissertation, decomposition of poly(ethylene oxide) loaded with different concentrations of pristine graphene and graphene oxide nano-platelets under extremely high temperature condition were investigated using reactive molecular dynamics simulation. The onset of non-isothermal decomposition of the pristine graphene-loaded poly(ethylene oxide) system was the highest among all systems, suggesting that introducing pristine graphene to the polymer improves its thermal stability (an effect that increases with an increase in the pristine graphene concentration). At low concentration, introducing graphene oxide to the polymer brings about a deterioration of the thermal stability of the polymer consistent with experimental findings. On average, the activation energy for the isothermal decomposition of pristine graphene-loaded poly(ethylene oxide) system increases by 60% over that of the neat poly(ethylene oxide) system, while it decreases by 40% for the graphene oxide-loaded poly(ethylene oxide) system. A time-dependent analysis of the through-thickness decomposition profile of the above systems reveals

that the polymer confined between the pristine graphene sheets exhibit a higher thermal stability compared to the bulk polymer. However, an opposite effect is observed with the polymer confined between the graphene oxide sheets. The latter observation is attributed to accelerated polymer chain scission in confined regions due to the ejection of reactive hydroxyl radicals from the graphene oxide surface during the early stages of thermal decomposition.

In The second part, a reactive molecular dynamics simulation was employed to compare between the damage mitigation efficacy of pristine and polyimide (PI)-grafted polyoctahedral silsesquioxane, graphene, and carbon nanotubes in a polyimide matrix exposed to extreme energetic atomic oxygen flux. The concentration of POSS and the orientation of graphene and carbon nanotube nanoparticles were further investigated. Overall, the mass loss, erosion yield, surface damage, atomic oxygen penetration depth, and temperature evolution are lower for the polyimide systems with randomly oriented carbon nanotubes and graphene or PI-grafted POSS compared to those of the pristine POSS or aligned carbon nanotubes and graphene systems at the same nanoparticle concentration. Based on experimental early degradation data (before the onset of nanoparticle damage), the amount of exposed polyimide, which has the highest erosion yield of all material components, on the material surface is the most important parameter affecting the erosion yield of the hybrid material. Our data indicate that the polyimide systems with randomly oriented carbon nanotubes and graphene nanoparticles have the lowest amount of exposed polyimide on the material surface; therefore, a lower erosion yield is obtained for these systems compared to those of the polyimide systems with aligned carbon nanotubes and graphene nanoparticles. However, the PI/grafted-POSS system has a significantly lower erosion yield than the polyimide systems with aligned carbon nanotubes and graphene nanoparticles, again due to a lower amount of exposed polyimide on the surface. When comparing the polyimide systems

loaded with PI-grafted POSS versus pristine POSS at low and high nanoparticle concentrations, our data indicate that grafting the POSS and increasing the POSS concentration lower the erosion yield by a factor of about 4 and 1.5, respectively. The former is attributed to a better dispersion of PI-grafted POSS versus that of the pristine POSS in the polyimide matrix, as determined by the radial distribution function.

In third part of this dissertation, molecular dynamics simulations were performed to determine thermal conductivities and through-thickness temperature profiles of unprotected crosslinked epoxy, as well as protected epoxy with graphene and montmorillonite/graphene surface coatings against lightning strike damage. Three hot surface temperatures of 500 K, 1,000 K, and 10,000 K, corresponding to the initial stages of the temperature rise at the lightning strike site, were used, while the cold surface was kept at 298 K. The MMT/Gr double-layer coating provided the most efficient thermal shielding of the epoxy sublayer, even at 10,000 K. Much less efficient thermal shielding was observed for Gr coating.

LIST OF REFERENCES

1. Wei, J., et al., *Thermal kinetics and thermo-mechanical properties of graphene integrated fluoroelastomer.* Journal of Polymer Science Part B: Polymer Physics, 2015. **53**(23): p. 1691-1700.
2. Kim, I.H. and Y.G. Jeong, *Polylactide/exfoliated graphite nanocomposites with enhanced thermal stability, mechanical modulus, and electrical conductivity.* Journal of Polymer Science Part B: Polymer Physics, 2010. **48**(8): p. 850-858.
3. Wang, X., et al., *Thermal degradation behaviors of epoxy resin/POSS hybrids and phosphorus–silicon synergism of flame retardancy.* Journal of Polymer Science Part B: Polymer Physics, 2010. **48**(6): p. 693-705.
4. Mittal, V., *Modeling and Prediction of Polymer Nanocomposite Properties*. 2012: Wiley.
5. Chen, E.J. and B.S. Hsiao, *The effects of transcrystalline interphase in advanced polymer composites.* Polymer Engineering & Science, 1992. **32**(4): p. 280-286.
6. Jesson, D.A. and J.F. Watts, *The interface and interphase in polymer matrix composites: Effect on mechanical properties and methods for identification.* Polymer Reviews, 2012. **52**(3): p. 321-354.
7. Nouranian, S., et al., *Molecular dynamics simulations of vinyl ester resin monomer interactions with a pristine vapor-grown carbon nanofiber and their implications for composite interphase formation.* Carbon, 2011. **49**(10): p. 3219-3232.
8. Jang, C., et al., *Molecular dynamics simulations of oxidized vapor-grown carbon nanofiber surface interactions with vinyl ester resin monomers.* Carbon, 2012. **50**(3): p. 748-760.
9. Alcoutlabi, M. and G.B. McKenna, *Effects of confinement on material behaviour at the nanometre size scale.* Journal of Physics: Condensed Matter, 2005. **17**(15): p. R461.

10. Rittigstein, P., et al., *Model polymer nanocomposites provide an understanding of confinement effects in real nanocomposites.* Nature materials, 2007. **6**(4): p. 278-282.

11. Stoliarov, S.I., et al., *A reactive molecular dynamics model of thermal decomposition in polymers: I. Poly (methyl methacrylate).* Polymer, 2003. **44**(3): p. 883-894.

12. Stoliarov, S.I., R.E. Lyon, and M.R. Nyden, *A reactive molecular dynamics model of thermal decomposition in polymers. II. Polyisobutylene.* Polymer, 2004. **45**(25): p. 8613-8621.

13. Nyden, M.R., et al., *Applications of reactive molecular dynamics to the study of the thermal decomposition of polymers and nanoscale structures.* Materials Science and Engineering A, 2004. **365**(1): p. 114-121.

14. Chenoweth, K., et al., *Simulations on the thermal decomposition of a poly (dimethylsiloxane) polymer using the ReaxFF reactive force field.* Journal Of The American Chemical Society, 2005. **127**(19): p. 7192-7202.

15. Diao, Z., et al., *ReaxFF reactive force field for molecular dynamics simulations of epoxy resin thermal decomposition with model compound.* Journal of Analytical and Applied Pyrolysis, 2013. **104**: p. 618-624.

16. Akhtar, M.S., et al., *High efficiency solid state dye sensitized solar cells with graphene–polyethylene oxide composite electrolytes.* Nanoscale, 2013. **5**(12): p. 5403-5411.

17. Lee, H.B., et al., *Preparation and characterization of poly (ethylene oxide)/graphene nanocomposites from an aqueous medium.* Journal of Macromolecular Science - Physics, 2010. **49**(4): p. 802-809.

18. Bai, X., Y. Zhai, and Y. Zhang, *Green approach to prepare graphene-based composites with high microwave absorption capacity.* The Journal of Physical Chemistry C, 2011. **115**(23): p. 11673-11677.

19. Mahmoud, W.E., *Morphology and physical properties of poly (ethylene oxide) loaded graphene nanocomposites prepared by two different techniques.* European Polymer Journal, 2011. **47**(8): p. 1534-1540.

20. Wang, C., et al., *Graphene oxide stabilized polyethylene glycol for heat storage.* Physical Chemistry Chemical Physics, 2012. **14**(38): p. 13233-13238.

21. Barroso-Bujans, F., et al., *Thermal stability of polymers confined in graphite oxide.* Macromolecules, 2013. **46**(5): p. 1890-1898.

22. Rahmani, F., et al., *Molecular simulation insights on the in vacuo adsorption of amino acids on graphene oxide surfaces with varying surface oxygen densities.* Journal of Nanoparticle Research, 2016. **18**(11): p. 320.

23. Mahdavi, M., F. Rahmani, and S. Nouranian, *Molecular simulation of pH-dependent diffusion, loading, and release of doxorubicin in graphene and graphene oxide drug delivery systems.* Journal of Materials Chemistry B, 2016. **4**(46): p. 7441-7451.

24. Sun, H., *COMPASS: An ab initio Force-Field Optimized for Condensed-phase Applications, Overview with Details on Alkane and Benzene Compounds.* The Journal of Physical Chemistry B, 1998. **102**(38): p. 7338-7364.

25. Plimpton, S., *Fast Parallel Algorithms for Short-Range Molecular Dynamics.* Journal of Computational Physics, 1995. **117**(1): p. 1-19.

26. Grippo, L. and S. Lucidi, *A globally convergent version of the Polak-Ribiere conjugate gradient method.* Mathematical Programming, 1997. **78**(3): p. 375-391.

27. Štich, I., et al., *Conjugate Gradient Minimization of the Energy Functional: A New Method for Electronic Structure Calculation.* Physical Review B, 1989. **39**(8): p. 4997.

28. Chenoweth, K., A.C.T. Van Duin, and W.A. Goddard III, *ReaxFF Reactive Force Field for Molecular Dynamics Simulations of Hydrocarbon Oxidation.* The Journal of Physical Chemistry A, 2008. **112**(5): p. 1040-1053.

29. Aktulga, H.M., et al., *Parallel reactive molecular dynamics: Numerical methods and algorithmic techniques.* Parallel Computing, 2012. **38**(4): p. 245-259.

30. Brenner, D.W., et al., *A second-generation reactive empirical bond order (REBO) potential energy expression for hydrocarbons.* Journal of Physics: Condensed Matter, 2002. **14**: p. 783.

31. Mun, S., et al., *An Interatomic Potential for Hydrocarbons Based on the Modified Embedded-Atom Method with Bond Order (MEAM-BO).* The Journal of Physical Chemistry A, 2017.

32. Senftle, T.P., et al., *The ReaxFF reactive force-field: development, applications and future directions.* npj Computational Materials, 2016. **2**: p. 15011.

33. Liu, X., et al., *Study of high density polyethylene (HDPE) pyrolysis with reactive molecular dynamics.* Polymer Degradation and Stability, 2014. **104**: p. 62-70.

34. Goverapet Srinivasan, S. and A.C. van Duin, *Molecular-dynamics-based study of the collisions of hyperthermal atomic oxygen with graphene using the ReaxFF reactive force field.* The Journal of Physical Chemistry A, 2011. **115**(46): p. 13269-13280.

35. Berendsen, H.J., et al., *Molecular dynamics with coupling to an external bath.* The Journal of chemical physics, 1984. **81**(8): p. 3684-3690.

36. Yang, L., et al., *A study of the mechanism of the oxidative thermal degradation of poly (ethylene oxide) and poly (propylene oxide) using 1 H-and 13 C-NMR.* European polymer journal, 1996. **32**(5): p. 535-547.

37. Zhou, T.-T. and F.-L. Huang, *Effects of defects on thermal decomposition of HMX via ReaxFF molecular dynamics simulations.* The Journal of Physical Chemistry B, 2010. **115**(2): p. 278-287.

38. Banks, B.A., K.K. de Groh, and S.K. Miller, *Low Earth Orbital Atomic Oxygen Interactions with Spacecraft Materials*. 2004, NASA Glenn Research Center: Cleveland, OH.

39. Samwel, S., *Low Earth Orbital Atomic Oxygen Erosion Effect on Spacecraft Materials.* Space Research Journal, 2014. **7**(1): p. 1-13.

40. Novikov, L.S., et al., *Atomic Oxygen Influence on Polymer Nanocomposites with Different Fillers.* Journal of Spacecraft and Rockets, 2016: p. 1-7.

41. Minton, T.K., et al., *Atomic Oxygen Effects on POSS Polyimides in Low Earth Orbit.* ACS applied materials & interfaces, 2012. **4**(2): p. 492-502.

42. Duo, S., et al., *Surface Modification of POSS–Polyimide Hybrid Films by Atomic Oxygen Using ECR Plasma.* Nuclear Instruments and Methods in Physical Research Section B, 2013. **307**: p. 324-327.

43. Duo, S., et al., *Atomic Oxygen Erosion Resistance of Polysiloxane/POSS Hybrid Coatings on Kapton.* Physics Procedia, 2013. **50**: p. 337-342.

44. Li, W.-p., H.-c. Liu, and L.-l. Feng, *Preparation and Anti Atomic Oxygen Erosion Properties of OPPOSS/PI Composites.* International Journal of Minerals, Metallurgy, and Materials, 2013. **20**(10): p. 994-1000.

45. Liu, Y., et al., *Characterization and Analysis on Atomic Oxygen Resistance of POSS/PVDF Composites.* Applied Surface Science, 2014. **320**: p. 908-913.

46. Zeng, F., et al., *Reactive Molecular Dynamics Simulations on the Disintegration of PVDF, FP-POSS, and Their Composite during Atomic Oxygen Impact.* The Journal of Physical Chemistry A, 2015. **119**(30): p. 8359-8368.

47. Fang, G., et al., *Intrinsically Atomic-oxygen Resistant POSS-containing Polyimide Aerogels: Synthesis and Characterization.* Chemistry Letters, 2015(0).

48. Lei, X., et al., *Evolution of Surface Chemistry and Morphology of Hyperbranched Polysiloxane Polyimides in Simulated Atomic Oxygen Environment.* Corrosion Science, 2015. **98**: p. 560-572.

49. Peng, D., W. Qin, and X. Wu, *A Study on Resistance to Ultraviolet Radiation of POSS–TiO2/Epoxy Nanocomposites.* Acta Astronautica, 2015. **111**: p. 84-88.

50. Jiao, L., et al., *Atomic Oxygen Exposure Behaviors of CVD-grown Carbon Nanotube Film and Its Polymer Composite Film.* Composites Part A Applied Science and Manufacturing, 2015. **71**: p. 116-125.

51. Atar, N., et al., *Atomic-oxygen-durable and Electrically-conductive CNT-POSS-Polyimide Flexible Films for Space Applications.* ACS applied materials & interfaces, 2015. **7**(22): p. 12047-12056.

52. Zhang, W., et al., *Graphene-reinforced Epoxy Resin with Enhanced Atomic Oxygen Erosion Resistance.* Journal of Materials Science, 2013. **48**(6): p. 2416-2423.

53. Wen, Z., et al., *Application of Graphene on Improving Atomic Oxygen Resistance of Material.* Journal of Beijing University of Aeronautics and Astronautics, 2014. **2**: p. 006.

54. Liu, L., et al., *Enhanced Atomic Oxygen Erosion Resistance and Mechanical Properties of Graphene/Cellulose Acetate Composite Films.* Journal of Applied Polymer Science, 2014. **131**(11).

55. Noh, J.-Y., S.-B. Jin, and C.-G. Kim, *Characteristics of Silane Treated Graphene Filled Nanocomposites Exposed to Low Earth Orbit Space Environment.* Composites Research, 2015. **28**(3): p. 130-135.

56. Chen, L., et al., *Processing and Characterization of ZnO Nanowire-Grown PBO Fibers with Simultaneously Enhanced Interfacial and Atomic Oxygen Resistance Properties.* RSC Advances, 2014. **4**(104): p. 59869-59876.

57. Lv, M., et al., *Effects of Atomic Oxygen Exposure on the Tribological Performance of ZrO2-Reinforced Polyimide Nanocomposites for Low Earth Orbit Space Applications.* Composites Part B Engineering, 2015. **77**: p. 215-222.

58. Yi, M., et al., *Hydrodynamics-assisted Scalable Production of Boron Nitride Nanosheets and Their Application in Improving Oxygen-atom Erosion Resistance of Polymeric Composites.* Nanoscale, 2013. **5**(21): p. 10660-10667.

59. Banks, B.A., et al., *Prediction of Atomic Oxygen Erosion Yield for Spacecraft Polymers.* Journal of Spacecraft and Rockets, 2011. **48**(1): p. 14-22.

60. Paci, J.T., et al., *Theoretical and Experimental Studies of the Reactions between Hyperthermal O(3P) and Graphite: Graphene-Based Direct Dynamics and Beam-Surface Scattering Approaches.* The Journal of Physical Chemistry A, 2009. **113**(16): p. 4677-4685.

61. Voronina, E., et al., *Mathematical and Experimental Simulation of Impact of Atomic Oxygen of the Earth's Upper Atmosphere on Nanostructures and Polymer Composites.* Inorganic Materials: Applied Research, 2012. **3**(2): p. 95-101.

62. Goverapet Srinivasan, S. and A.C.T. van Duin, *Molecular-Dynamics-Based Study of the Collisions of Hyperthermal Atomic Oxygen with Graphene Using the ReaxFF Reactive Force Field.* The Journal of Physical Chemistry A, 2011. **115**(46): p. 13269-13280.

63. Rahnamoun, A. and A. van Duin, *Reactive Molecular Dynamics Simulation on the Disintegration of Kapton, POSS Polyimide, Amorphous Silica, and Teflon during Atomic Oxygen Impact Using the Reaxff Reactive Force-Field Method.* The Journal of Physical Chemistry A, 2014. **118**(15): p. 2780-2787.

64. Evans, D.J. and B.L. Holian, *The Nose–Hoover Thermostat.* The Journal of chemical physics, 1985. **83**(8): p. 4069-4074.

65. Van Duin, A.C.T., et al., *ReaxFF: A Reactive Force Field for Hydrocarbons.* The Journal of Physical Chemistry A, 2001. **105**(41): p. 9396-9409.

66. Zaminpayma, E., *Molecular Dynamics Simulation of Mechanical Properties and Interaction Energy of Polythiophene/Polyethylene/Poly (p-phenylenevinylene) and CNTs Composites.* Polymer Composites, 2014. **35**(11): p. 2261-2268.

67. Van Duin, A.C., et al., *ReaxFFSiO reactive force field for silicon and silicon oxide systems.* The Journal of Physical Chemistry A, 2003. **107**(19): p. 3803-3811.

68. Balazs, A.C., T. Emrick, and T.P. Russell, *Nanoparticle Polymer Composites: Where Two Small Worlds Meet.* Science, 2006. **314**(5802): p. 1107-1110.

69. De Groh, K.K., et al., *MISSE 2 PEACE Polymers Atomic Oxygen Erosion Experiment on the International Space Station.* High Performance Polymers, 2008. **20**(4-5): p. 388-409.

70. Nicholson, K.T., T.K. Minton, and S. Sibener, *Temperature-dependent Morphological Evolution of HOPG Graphite Upon Exposure to Hyperthermal O (3P) Atoms.* Progress in organic coatings, 2003. **47**(3): p. 443-447.

71. Klomp-de Boer, R. and M. Smeets, *Lightning strike behaviour of thick walled composite parts.* 2013.

72. Mangalgiri, P., *Composite materials for aerospace applications.* Bulletin of Materials Science, 1999. **22**(3): p. 657-664.

73. Shahil, K.M. and A.A. Balandin, *Thermal properties of graphene and multilayer graphene: Applications in thermal interface materials.* Solid State Communications, 2012. **152**(15): p. 1331-1340.

74. Uddin, F., *Clays, nanoclays, and montmorillonite minerals.* Metallurgical and Materials Transactions A, 2008. **39**(12): p. 2804-2814.

75. Alamusi, et al., *Molecular dynamics simulations of thermal expansion properties of single layer graphene sheets.* Molecular Simulation, 2018. **44**(1): p. 34-39.

76. Sun, Y., et al., *Molecular dynamics simulation of the effect of oxygen-containing functional groups on the thermal conductivity of reduced graphene oxide.* Computational Materials Science, 2018. **148**: p. 176-183.

77. Teng, C.-C., et al., *Thermal conductivity and structure of non-covalent functionalized graphene/epoxy composites.* Carbon, 2011. **49**(15): p. 5107-5116.

78. Bozkurt, E., E. Kaya, and M. Tanoğlu, *Mechanical and thermal behavior of non-crimp glass fiber reinforced layered clay/epoxy nanocomposites.* Composites Science and Technology, 2007. **67**(15-16): p. 3394-3403.

79. Dauber-Osguthorpe, P., et al., *Structure and energetics of ligand binding to proteins: Escherichia coli dihydrofolate reductase-trimethoprim, a drug-receptor system.* Proteins: Structure, Function, and Bioinformatics, 1988. **4**(1): p. 31-47.

80. Awasthi, A.P., D.C. Lagoudas, and D.C. Hammerand, *Modeling of graphene–polymer interfacial mechanical behavior using molecular dynamics.* Modelling and Simulation in Materials Science and Engineering, 2008. **17**(1): p. 015002.

81. Karataş, D., et al., *Interaction of curcumin in a drug delivery system including a composite with poly (lactic-co-glycolic acid) and montmorillonite: a density functional theory and molecular dynamics study.* Journal of Materials Chemistry B, 2017. **5**(40): p. 8070-8082.

82. Payne, M.C., et al., *Iterative minimization techniques for ab initio total-energy calculations: molecular dynamics and conjugate gradients.* Reviews of modern physics, 1992. **64**(4): p. 1045.

83. Andersen, H.C., *Molecular dynamics simulations at constant pressure and/or temperature.* The Journal of chemical physics, 1980. **72**(4): p. 2384-2393.

84. Gournis, D., et al., *A neutron diffraction study of alkali cation migration in montmorillonites.* Physics and Chemistry of Minerals, 2008. **35**(1): p. 49-58.

85. Müller-Plathe, F., *A simple nonequilibrium molecular dynamics method for calculating the thermal conductivity.* The Journal of chemical physics, 1997. **106**(14): p. 6082-6085.

LIST OF APPENDICES

APPENDIX A: ReaxFF Parameter Set of poly(ethylene oxide)/graphene nanocomposites
APPENDIX B: Polyimide Coatings Exposed to Atomic Oxygen Bombardment

APPENDIX A: ReaxFF Parameter Set of poly(ethylene oxide)/graphene nanocomposites

Reactive MD-force field

39 ! Number of general parameters

50.0000 !Overcoordination parameter

9.5469 !Overcoordination parameter

127.8302 !Valency angle conjugation parameter

3.0000 !Triple bond stabilisation parameter

6.5000 !Triple bond stabilisation parameter

0.0000 !C2-correction

1.0496 !Undercoordination parameter

9.0000 !Triple bond stabilisation parameter

11.5054 !Undercoordination parameter

13.4059 !Undercoordination parameter

0.0000 !Triple bond stabilization energy

0.0000 !Lower Taper-radius

10.0000 !Upper Taper-radius

2.8793 !Not used

33.8667 !Valency undercoordination

7.0994 !Valency angle/lone pair parameter

1.0563 !Valency angle

2.0384 !Valency angle parameter

6.1431 !Not used

6.9290 !Double bond/angle parameter

```
 0.3989 !Double bond/angle parameter: overcoord
 3.9954 !Double bond/angle parameter: overcoord
-2.4837 !Not used
 5.7796 !Torsion/BO parameter
10.0000 !Torsion overcoordination
 1.9487 !Torsion overcoordination
-1.2327 !Conjugation 0 (not used)
 2.1645 !Conjugation
 1.5591 !vdWaals shielding
 0.1000 !Cutoff for bond order (*100)
 2.0038 !Valency angle conjugation parameter
 0.6121 !Overcoordination parameter
 1.2172 !Overcoordination parameter
 1.8512 !Valency/lone pair parameter
 0.5000 !Not used
20.0000 !Not used
 5.0000 !Molecular energy (not used)
 0.0000 !Molecular energy (not used)
 3.6942 !Valency angle conjugation parameter
 5    ! Nr of atoms; cov.r; valency;a.m;Rvdw;Evdw;gammaEEM;cov.r2;#
        alfa;gammavdW;valency;Eunder;Eover;chiEEM;etaEEM;n.u.
        cov r3;Elp;Heat inc.;n.u.;n.u.;n.u.;n.u.
        ov/un;val1;n.u.;val3,vval4
C    1.3763   4.0000  12.0000   1.8857   0.1818   0.8712   1.2596   4.0000
     9.5928   2.0784   4.0000  22.6732  79.5548   5.7254   6.9235   0.0000
     1.2065   0.0000  -0.8579   4.9417  28.3475  11.9957   0.8563   0.0000
    -2.8846   4.1590   1.0564   4.0000   2.9663   0.0000   0.0000   0.0000
H    0.6646   1.0000   1.0080   1.6030   0.0600   0.7625  -0.1000   1.0000
```

```
    9.3951   4.4187   1.0000   0.0000 121.1250   3.8196   9.8832   1.0000
   -0.1000   0.0000  -0.1339   3.5803   2.8733   1.0000   1.0698   0.0000
  -13.0615   3.0626   1.0338   1.0000   2.8793   0.0000   0.0000   0.0000
O   1.2699   2.0000  15.9990   1.9741   0.0880   1.0804   1.0624   6.0000
   10.2186   7.7719   4.0000  27.3264 116.0768   8.5000   7.8386   2.0000
    0.9446   8.6170  -1.2371  17.0845   3.7082   0.5350   0.9745   0.0000
   -3.1456   2.6656   1.0493   4.0000   2.9225   0.0000   0.0000   0.0000
N   1.2226   3.0000  14.0000   1.9324   0.1376   0.8596   1.1839   5.0000
   10.0667   7.8431   4.0000  32.5000 100.0000   6.8418   6.3404   2.0000
    1.0497  14.5853  -1.1222   2.0637   3.2584   3.1136   0.9745   0.0000
   -4.2059   2.6491   1.0183   4.0000   2.8793   0.0000   0.0000   0.0000
S   1.9405   2.0000  32.0600   2.0677   0.2099   1.0336   1.5479   6.0000
    9.9575   4.9055   4.0000  52.9998 112.1416   6.5000   8.2545   2.0000
    1.4601   9.7177  -2.3700   5.7487  23.2859  12.7147   0.9745   0.0000
  -11.0000   2.7466   1.0338   4.0000   2.8793   0.0000   0.0000   0.0000
15      ! Nr of bonds; Edis1;LPpen;n.u.;pbe1;pbo5;13corr;pbo6
                    pbe2;pbo3;pbo4;n.u.;pbo1;pbo2;ovcorr
 1  1 145.4070 103.0681  73.7841   0.2176  -0.7816   1.0000  28.4167   0.3217
       0.1111  -0.1940   8.6733   1.0000  -0.0994   5.9724   1.0000   0.0000
 1  2 167.1752   0.0000   0.0000  -0.4421   0.0000   1.0000   6.0000   0.5969
      17.4194   1.0000   0.0000   1.0000  -0.0099   8.5445   0.0000   0.0000
 2  2 188.1606   0.0000   0.0000  -0.3140   0.0000   1.0000   6.0000   0.6816
       8.6247   1.0000   0.0000   1.0000  -0.0183   5.7082   0.0000   0.0000
 1  3 171.0470  67.2480 130.3792   0.3600  -0.1696   1.0000  12.0338   0.3796
       0.3647  -0.2660   7.4396   1.0000  -0.1661   5.0637   0.0000   0.0000
 3  3  90.2465 160.9645  40.0000   0.9950  -0.2435   1.0000  28.1614   0.9704
       0.8145  -0.1850   7.5281   1.0000  -0.1283   6.2396   1.0000   0.0000
 1  4 134.9992 139.6314  78.5681   0.0420  -0.1370   1.0000  23.6247   0.2415
```

```
      0.1522  -0.3161   7.0000   1.0000  -0.1301   5.4980   1.0000   0.0000
 3  4 127.7074 177.1058  40.0000   0.4561  -0.1481   1.0000  31.4801   0.2000
      0.8968  -0.3555   7.0000   1.0000  -0.1219   7.0000   1.0000   0.0000
 4  4 151.9142  87.1928 151.4761   0.4280  -0.1001   1.0000  12.3631   0.6229
      0.1721  -0.1614  12.1345   1.0000  -0.0882   5.3056   1.0000   0.0000
 2  3 216.6018   0.0000   0.0000  -0.4201   0.0000   1.0000   6.0000   0.9143
      4.7737   1.0000   0.0000   1.0000  -0.0591   5.9451   0.0000   0.0000
 2  4 223.1853   0.0000   0.0000  -0.4661   0.0000   1.0000   6.0000   0.5178
      7.8731   1.0000   0.0000   1.0000  -0.0306   6.1506   0.0000   0.0000
 1  5 128.9942  74.5848  55.2528   0.1035  -0.5211   1.0000  18.9617   0.6000
      0.2949  -0.2398   8.1175   1.0000  -0.1029   5.6731   1.0000   0.0000
 2  5 151.5159   0.0000   0.0000  -0.4721   0.0000   1.0000   6.0000   0.6000
      9.4366   1.0000   0.0000   1.0000  -0.0290   7.0050   1.0000   0.0000
 3  5   0.0000   0.0000   0.0000   0.5563  -0.4038   1.0000  49.5611   0.6000
      0.4259  -0.4577  12.7569   1.0000  -0.1100   7.1145   1.0000   0.0000
 4  5   0.0000   0.0000   0.0000   0.4438  -0.2034   1.0000  40.3399   0.6000
      0.3296  -0.3153   9.1227   1.0000  -0.1805   5.6864   1.0000   0.0000
 5  5  96.1871  93.7006  68.6860   0.0955  -0.4781   1.0000  17.8574   0.6000
      0.2723  -0.2373   9.7875   1.0000  -0.0950   6.4757   1.0000   0.0000
 6    ! Nr of off-diagonal terms; Ediss;Ro;gamma;rsigma;rpi;rpi2
 1  2   0.0455   1.7218  10.4236   1.0379  -1.0000  -1.0000
 2  3   0.0469   1.9185  10.3707   0.9406  -1.0000  -1.0000
 2  4   0.0999   1.8372   9.6539   0.9692  -1.0000  -1.0000
 1  3   0.1186   1.9820   9.5927   1.2936   1.1203   1.0805
 1  4   0.1486   1.8922   9.7989   1.3746   1.2091   1.1427
 3  4   0.1051   2.0060  10.0691   1.3307   1.1034   1.0060
50    ! Nr of angles;at1;at2;at3;Thetao,o;ka;kb;pv1;pv2
 1  1  1  70.0265  13.6338   2.1884   0.0000   0.1676  26.3587   1.0400
```

1 1 2 69.7786 10.3544 8.4326 0.0000 0.1153 0.0000 1.0400

2 1 2 74.6020 11.8629 2.9294 0.0000 0.1367 0.0000 1.0400

1 2 2 0.0000 0.0000 6.0000 0.0000 0.0000 0.0000 1.0400

1 2 1 0.0000 3.4110 7.7350 0.0000 0.0000 0.0000 1.0400

2 2 2 0.0000 27.9213 5.8635 0.0000 0.0000 0.0000 1.0400

1 1 3 72.9588 16.7105 3.5244 0.0000 1.1127 0.0000 1.1880

3 1 3 80.0708 45.0000 2.1487 0.0000 1.1127 -35.0000 1.1880

1 1 4 61.5055 45.0000 1.2242 0.0000 1.1127 0.0000 1.1880

3 1 4 71.9345 45.0000 1.5052 0.0000 1.1127 0.0000 1.1880

4 1 4 51.3604 45.0000 0.6846 0.0000 1.1127 0.0000 1.1880

2 1 3 66.6150 13.6403 3.8212 0.0000 0.0755 0.0000 1.0500

2 1 4 68.9632 16.3575 3.1449 0.0000 0.0755 0.0000 1.0500

1 2 4 0.0000 0.0019 6.3000 0.0000 0.0000 0.0000 1.0400

1 3 1 79.1091 45.0000 0.7067 0.0000 0.6142 0.0000 1.0783

1 3 3 83.7151 42.6867 0.9699 0.0000 0.6142 0.0000 1.0783

1 3 4 79.5876 45.0000 1.1761 0.0000 0.6142 0.0000 1.0783

3 3 3 80.0108 38.3716 1.1572 -38.4200 0.6142 0.0000 1.0783

3 3 4 81.5614 19.8012 3.9968 0.0000 0.6142 0.0000 1.0783

4 3 4 85.3564 36.5858 1.7504 0.0000 0.6142 0.0000 1.0783

1 3 2 78.1533 44.7226 1.3136 0.0000 0.1218 0.0000 1.0500

2 3 3 84.1057 9.6413 7.5000 0.0000 0.1218 0.0000 1.0500

2 3 4 79.4629 44.0409 2.2959 0.0000 0.1218 0.0000 1.0500

2 3 2 79.2954 26.3838 2.2044 0.0000 0.1218 0.0000 1.0500

1 4 1 66.1477 22.9891 1.5923 0.0000 1.6777 0.0000 1.0500

1 4 3 91.9273 38.0207 0.5387 0.0000 1.6777 0.0000 1.0500

1 4 4 92.6933 9.9708 1.6094 0.0000 1.6777 0.0000 1.0500

3 4 3 73.4749 42.7640 1.7325 -17.5007 1.6777 0.0000 1.0500

3 4 4 73.9183 44.8857 1.1980 -0.9193 1.6777 0.0000 1.0500

4 4 4 74.0572 15.4709 5.4220 0.0000 1.6777 0.0000 1.0500

1 4 2 72.7016 33.4153 1.0224 0.0000 0.0222 0.0000 1.0500

2 4 3 82.4368 44.1900 1.9273 0.0000 0.0222 0.0000 1.0500

2 4 4 82.6883 39.9831 1.1916 0.0000 0.0222 0.0000 1.0500

2 4 2 71.2183 14.4528 3.6870 0.0000 0.0222 0.0000 1.0500

1 2 3 0.0000 0.0019 6.0000 0.0000 0.0000 0.0000 1.0400

1 2 4 0.0000 0.0019 6.0000 0.0000 0.0000 0.0000 1.0400

1 2 5 0.0000 0.0019 6.0000 0.0000 0.0000 0.0000 1.0400

3 2 3 0.0000 0.0019 6.0000 0.0000 0.0000 0.0000 1.0400

3 2 4 0.0000 0.0019 6.0000 0.0000 0.0000 0.0000 1.0400

4 2 4 0.0000 0.0019 6.0000 0.0000 0.0000 0.0000 1.0400

2 2 3 0.0000 0.0019 6.0000 0.0000 0.0000 0.0000 1.0400

2 2 4 0.0000 0.0019 6.0000 0.0000 0.0000 0.0000 1.0400

1 1 5 74.9397 25.0560 1.8787 0.1463 0.0559 0.0000 1.0400

1 5 1 86.9521 36.9951 2.0903 0.1463 0.0559 0.0000 1.0400

2 1 5 74.9397 25.0560 1.8787 0.0000 0.0000 0.0000 1.0400

1 5 2 86.1791 36.9951 2.0903 0.0000 0.0000 0.0000 1.0400

1 5 5 85.3644 36.9951 2.0903 0.1463 0.0559 0.0000 1.0400

2 5 2 93.1959 36.9951 2.0903 0.0000 0.0000 0.0000 1.0400

2 5 5 84.3331 36.9951 2.0903 0.0000 0.0000 0.0000 1.0400

2 2 5 0.0000 0.0019 6.0000 0.0000 0.0000 0.0000 1.0400

17 ! Nr of torsions;at1;at2;at3;at4;;V1;V2;V3;V2(BO);vconj;n.u;n

1 1 1 1 0.0000 23.2168 0.1811 -4.6220 -1.9387 0.0000 0.0000

1 1 1 2 0.0000 45.7984 0.3590 -5.7106 -2.9459 0.0000 0.0000

2 1 1 2 0.0000 44.6445 0.3486 -5.1725 -0.8717 0.0000 0.0000

0 1 2 0 0.0000 0.0000 0.0000 0.0000 0.0000 0.0000 0.0000

0 2 2 0 0.0000 0.0000 0.0000 0.0000 0.0000 0.0000 0.0000

0 1 3 0 5.0520 16.7344 0.5590 -3.0181 -2.0000 0.0000 0.0000

0 2 3 0 0.0000 0.1000 0.0200 -2.5415 0.0000 0.0000 0.0000

0 3 3 0 0.0115 68.9706 0.8253 -28.4693 0.0000 0.0000 0.0000

0 1 4 0 -4.0616 66.2036 0.3855 -4.4414 -2.0000 0.0000 0.0000

0 2 4 0 0.0000 0.1000 0.0200 -2.5415 0.0000 0.0000 0.0000

0 3 4 0 1.1130 14.8049 0.0231 -10.7175 -2.0000 0.0000 0.0000

0 4 4 0 -0.0851 37.4200 0.0107 -3.5209 -2.0000 0.0000 0.0000

0 1 1 0 0.0000 0.9305 0.0000 -24.2568 0.0000 0.0000 0.0000

4 1 4 4 -3.6064 43.6430 0.0004 -11.5507 -2.0000 0.0000 0.0000

0 1 5 0 3.3423 30.3435 0.0365 -2.7171 0.0000 0.0000 0.0000

0 5 5 0 -0.0555 -42.7738 0.1515 -2.2056 0.0000 0.0000 0.0000

0 2 5 0 0.0000 0.0000 0.0000 0.0000 0.0000 0.0000 0.0000

9 ! Nr of hydrogen bonds;at1;at2;at3;Rhb;Dehb;vhb1

3 2 3 2.0431 -6.6813 3.5000 1.7295

3 2 4 1.6740 -10.9581 3.5000 1.7295

4 2 3 1.4889 -9.6465 3.5000 1.7295

4 2 4 1.8324 -8.0074 3.5000 1.7295

3 2 5 2.6644 -3.9547 3.5000 1.7295

4 2 5 4.0476 -5.7038 3.5000 1.7295

5 2 3 2.1126 -4.5790 3.5000 1.7295

5 2 4 2.2066 -5.7038 3.5000 1.7295

5 2 5 1.9461 -4.0000 3.5000 1.7295

APPENDIX B: Polyimide Coatings Exposed to Atomic Oxygen Bombardment

B.1. Polymer Chain and Simulation Cell Size Effects

An investigation into the effects of polymer chain and simulation cell sizes on the relevant mass loss data were performed. For this purpose, three systems were created using the procedure outlined in the paper: 1) polyimide (PI) with one monomer unit per PI chain (designated as PI-Short-Chain) (240 total PI chains as given for the Neat PI system in Table 1), 2) PI with three monomer units per PI chain (PI-Long-Chain) (80 total PI chains, same size as that of the Neat PI system), and 3) PI with one monomer unit per PI chain (PI-Small-Cell) (120 total PI chains, size: 43×43×30 $Å^3$). The simulation procedure for these systems is similar to that of the other nanoparticle-loaded PI systems, as described in the paper. To improve the statistical sampling of the data, a total of three simulations were performed for each system and the mass loss data were averaged over all simulations.

The average normalized mass loss data for the above systems are shown in Fig. S1. As seen in this figure, the system with the larger polymer chains (PI-Long-Chain) has a negligibly higher onset of mass loss versus that of the PI-Short-Chain system. When decreasing the simulation cell size at constant polymer chain size, the onsets of mass loss are similar; however, there is a slight increase in the rate of degradation for the PI-Small-Cell system. While size effects may be present for the systems studied in this work, it is anticipated that these effects are small relative to the

phenomena investigated, i.e., atomic oxygen (AO) penetration depth, damage propagation depth (DPD), erosion, etc. Indeed., the calculated AO penetration depth and DPD for all material systems in this work are smaller than the *z*-dimension of the respective simulation cells. This signifies the fact that our selected system sizes are appropriate in this work to observe the AO damage phenomena.

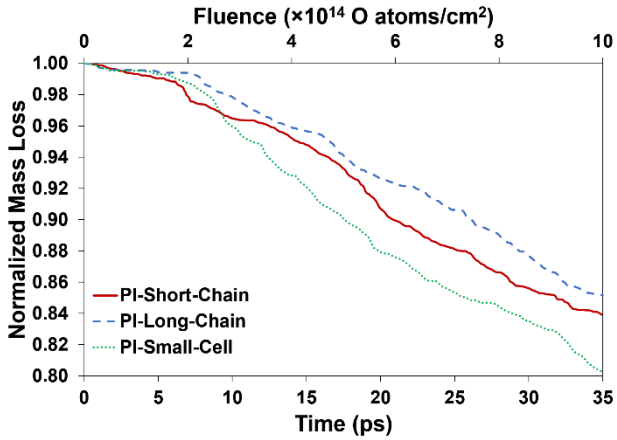

Figure B. 1. Averaged normalized mass loss as a function of simulation time for the Neat PI systems with short (PI-Short-Chain) and long (PI-Long-Chain) polymer chains at constant cell size, as well as short chains with smaller cell size (PI-Small-Cell).

B.2. Relative Density Distributions

Equilibrium relative density (ρ/ρ_{bulk}) distribution of systems are given in Figure S2.

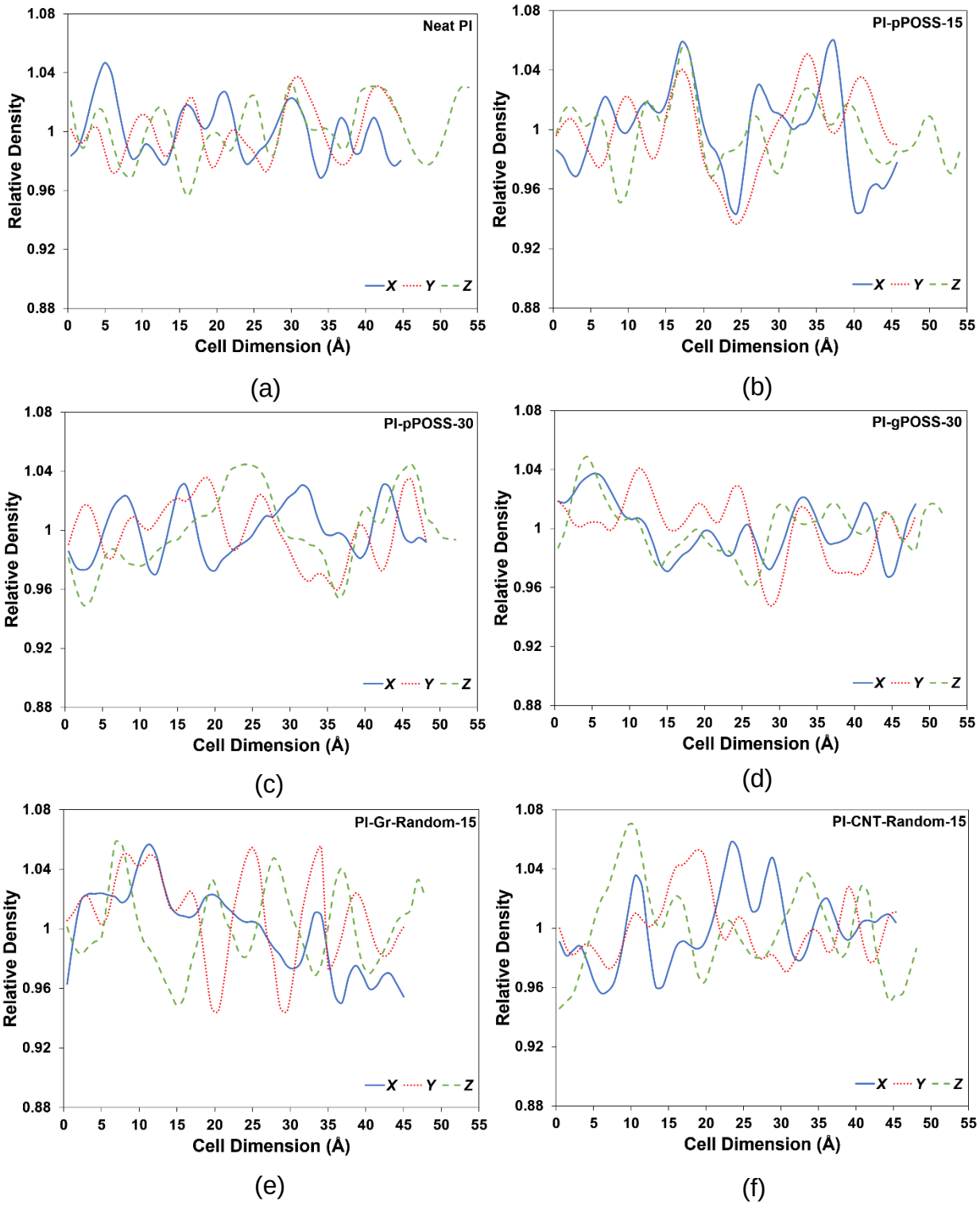

Figure B. 3. Relative density (ρ/ρ_{bulk}) distribution in the simulation cells for (a) Neat PI, (b) PI-pPOSS (15 wt%), (c) PI-pPOSS (30 wt%), (d) PI-gPOSS (30 wt%), (e) PI-Gr-Random, and (f) PI-CNT-Random systems after 2 ns of equilibration.

B.3. ReaxFF Parameter Set

Reactive MD-force field

```
 39      ! Number of general parameters
  50.0000 !Overcoordination parameter
   9.4514 !Overcoordination parameter
  29.8953 !Valency angle conjugation parameter
 216.5421 !Triple bond stabilisation parameter
  12.2245 !Triple bond stabilisation parameter
   0.0000 !C2-correction
   1.0701 !Undercoordination parameter
   7.5000 !Triple bond stabilisation parameter
  11.9083 !Undercoordination parameter
  13.3822 !Undercoordination parameter
 -10.9834 !Triple bond stabilization energy
   0.0000 !Lower Taper-radius
  10.0000 !Upper Taper-radius
   2.8793 !Not used
  33.8667 !Valency undercoordination
   3.3976 !Valency angle/lone pair parameter
   1.0563 !Valency angle
   2.0384 !Valency angle parameter
   6.1431 !Not used
   6.9290 !Double bond/angle parameter
```

```
 0.0283 !Double bond/angle parameter: overcoord
 0.0570 !Double bond/angle parameter: overcoord
-2.4837 !Not used
 5.8374 !Torsion/BO parameter
10.0000 !Torsion overcoordination
 1.8820 !Torsion overcoordination
-1.2327 !Conjugation 0 (not used)
 2.1861 !Conjugation
 1.5591 !vdWaals shielding
 0.0100 !Cutoff for bond order (*100)
 4.8414 !Valency angle conjugation parameter
 3.5857 !Overcoordination parameter
38.6472 !Overcoordination parameter
 2.1533 !Valency/lone pair parameter
 0.5000 !Not used
 1.0000 !Scale factor (d) in dispersion
 5.0000 !Molecular energy (not used)
 0.0000 !Molecular energy (not used)
6.9784 !Valency angle conjugation parameter
 7    ! Nr of atoms; cov.r; valency;a.m;Rvdw;Evdw;gammaEEM;cov.r2;#
        alfa;gammavdW;valency;Eunder;Eover;chiEEM;etaEEM;n.u.
        cov r3;Elp;Heat inc.;n.u.;n.u.;n.u.;n.u.
        ov/un;val1;n.u.;val3,vval4
```

C 1.3742 4.0000 12.0000 1.9684 0.1723 0.8712 1.2385 4.0000
8.7696 0.1000 4.0000 31.0823 79.5548 5.7254 6.9235 0.0000
1.2104 0.0000 183.8108 5.7419 33.3951 11.9957 0.8563 0.0000
-2.8983 4.7820 1.0564 4.0000 2.9663 1.6737 0.1421 14.0707
H 0.6867 1.0000 1.0080 1.3525 0.0616 0.8910 -0.1000 1.0000
9.1506 0.1000 1.0000 0.0000 121.1250 3.8446 10.0839 1.0000
-0.1000 0.0000 58.4369 3.8461 3.2540 1.0000 1.0698 0.0000
-15.7683 2.1504 1.0338 1.0000 2.8793 1.2669 0.0139 12.4538
O 1.3142 2.0000 15.9990 1.9741 0.0880 0.8712 1.1139 6.0000
9.9926 0.1000 4.0000 29.5271 116.0768 8.5000 7.1412 2.0000
0.9909 14.7235 69.2921 9.1371 1.6258 0.1863 0.9745 0.0000
-3.5965 2.5000 1.0493 4.0000 2.9225 1.7221 0.1670 13.9991
N 1.2456 3.0000 14.0000 2.0437 0.1035 0.8712 1.1911 5.0000
9.8823 0.1000 4.0000 32.4758 100.0000 6.8453 6.8349 2.0000
1.0636 0.0276 127.9672 2.2169 2.8632 2.4419 0.9745 0.0000
-4.0959 2.0047 1.0183 4.0000 2.8793 1.5967 0.1649 13.9888
S 1.9647 2.0000 32.0600 2.0783 0.2176 1.0336 1.5386 6.0000
9.9676 0.0812 4.0000 35.1648 112.1416 6.5000 8.2545 2.0000
1.4703 9.4922 70.0338 8.5146 28.0801 8.5010 0.9745 0.0000
-10.0773 2.7466 1.0338 6.2998 2.8793 1.5967 0.1649 13.9888
Si 2.0276 4.0000 28.0600 2.2042 0.1322 0.8218 1.5758 4.0000
11.9413 0.0618 4.0000 11.8211 136.4845 1.8038 7.3852 0.0000
-1.0000 0.0000 126.5331 6.4918 8.5961 0.2368 0.8563 0.0000

-3.8112 3.1873 1.0338 4.0000 2.5791 1.0000 0.1649 13.9888

X -0.1000 2.0000 1.0080 2.0000 0.0000 1.0000 -0.1000 6.0000

10.0000 0.5000 4.0000 0.0000 0.0000 8.5000 1.5000 0.0000

-0.1000 0.0000 -2.3700 8.7410 13.3640 0.6690 0.9745 0.0000

-11.0000 2.7466 1.0338 4.0000 2.8793 1.5967 0.1649 13.9888

20 ! Nr of bonds; Edis1;LPpen;n.u.;pbe1;pbo5;13corr;pbo6

pbe2;pbo3;pbo4;Etrip;pbo1;pbo2;ovcorr

1 1 141.9346 113.4487 67.6027 0.1554 -0.3045 1.0000 30.4515 0.4283

0.0801 -0.2113 8.5395 1.0000 -0.0933 6.6967 1.0000 0.0000

1 2 155.7526 0.0000 0.0000 -0.4525 0.0000 1.0000 6.0000 0.5921

12.1053 1.0000 0.0000 1.0000 -0.0097 8.6351 0.0000 0.0000

2 2 169.8421 0.0000 0.0000 -0.3591 0.0000 1.0000 6.0000 0.7503

9.3119 1.0000 0.0000 1.0000 -0.0169 5.9406 0.0000 0.0000

1 3 157.7219 89.8921 27.9315 -0.4324 -0.1742 1.0000 15.0019 0.5160

1.2934 -0.3079 7.0252 1.0000 -0.1543 4.5116 0.0000 0.0000

3 3 108.9631 158.3501 42.0558 0.1226 -0.1324 1.0000 28.5716 0.2545

1.0000 -0.2656 8.6489 1.0000 -0.1000 6.8482 1.0000 0.0000

1 4 128.9104 171.2945 100.5836 -0.1306 -0.4948 1.0000 26.7458 0.4489

0.3746 -0.3549 7.0000 1.0000 -0.1248 4.9232 1.0000 0.0000

3 4 76.1062 118.8680 75.7263 0.7080 -0.1062 1.0000 16.6913 0.2407

0.3535 -0.1906 8.4054 1.0000 -0.1154 5.6575 1.0000 0.0000

4 4 160.6599 73.3721 154.2849 -0.7107 -0.1462 1.0000 12.0000 0.6826

0.9330 -0.1434 10.6712 1.0000 -0.0890 4.6486 1.0000 0.0000

2 3 230.7607 0.0000 0.0000 -0.6643 0.0000 1.0000 6.0000 0.9854

5.1146 1.0000 0.0000 1.0000 -0.0532 5.1189 0.0000 0.0000

2 4 208.0443 0.0000 0.0000 -0.3923 0.0000 1.0000 6.0000 0.3221

10.5505 1.0000 0.0000 1.0000 -0.0690 6.2949 0.0000 0.0000

1 5 128.7959 56.4134 39.0716 0.0688 -0.4463 1.0000 31.1766 0.4530

0.1955 -0.3587 6.2148 1.0000 -0.0770 6.6386 1.0000 0.0000

2 5 128.6090 0.0000 0.0000 -0.5555 0.0000 1.0000 6.0000 0.4721

10.8735 1.0000 0.0000 1.0000 -0.0242 9.1937 1.0000 0.0000

3 5 0.0000 0.0000 0.0000 0.5563 -0.4038 1.0000 49.5611 0.6000

0.4259 -0.4577 12.7569 1.0000 -0.1100 7.1145 1.0000 0.0000

4 5 0.0000 0.0000 0.0000 0.4438 -0.2034 1.0000 40.3399 0.6000

0.3296 -0.3153 9.1227 1.0000 -0.1805 5.6864 1.0000 0.0000

5 5 96.1871 93.7006 68.6860 0.0955 -0.4781 1.0000 17.8574 0.6000

0.2723 -0.2373 9.7875 1.0000 -0.0950 6.4757 1.0000 0.0000

6 6 109.1904 70.8314 30.0000 0.2765 -0.3000 1.0000 16.0000 0.1583

0.2804 -0.1994 8.1117 1.0000 -0.2675 6.2993 0.0000 0.0000

2 6 137.0000 0.0000 0.0000 -0.1902 0.0000 1.0000 6.0000 0.2256

17.7186 1.0000 0.0000 1.0000 -0.0377 6.4281 0.0000 0.0000

3 6 136.6643 41.8662 0.0000 0.2527 -0.3000 1.0000 36.0000 0.6764

0.9938 -0.3800 10.3140 1.0000 -0.1915 6.2189 1.0000 0.0000

1 6 125.8776 57.9428 0.0000 0.1077 -0.5558 1.0000 17.2117 0.4687

0.2379 -0.3297 10.4455 1.0000 -0.1529 6.2959 1.0000 0.0000

4 6 103.7982 30.4010 20.2000 -0.1419 -0.3025 1.0000 35.5000 0.4217

```
      0.9927  -0.3060   9.9500   1.0000  -0.1654   8.3456   1.0000   0.0000
12    ! Nr of off-diagonal terms; Ediss;Ro;gamma;rsigma;rpi;rpi2
 1  2   0.0464   1.8296   9.9214   1.0029  -1.0000  -1.0000   0.0000
 2  3   0.0403   1.6913  10.4801   0.8774  -1.0000  -1.0000   0.0000
 2  4   0.0524   1.7325  10.1306   0.9982  -1.0000  -1.0000 294.9500
 1  3   0.1028   1.9277   9.1521   1.3399   1.1104   1.1609 631.8500
 1  4   0.2070   1.7366   9.5916   1.2960   1.2008   1.1262 650.0000
 3  4   0.0491   1.7025  10.6101   1.3036   1.1276   1.0173 880.0000
 1  6   0.0937   1.9583  11.0607   1.8627   1.5560  -1.0000 600.0000
 2  6   0.0470   1.6738  11.6877   1.0031  -1.0000  -1.0000   0.0000
 3  6   0.1263   1.6593  10.6833   1.5650   1.4452  -1.0000   0.0000
 4  6   0.1100   1.7548  10.9719   1.7231   1.4584  -1.0000 180.0000
 1  5   0.1408   1.8161   9.9393   1.7986   1.3021   1.4031   0.0000
 2  5   0.0895   1.6239  10.0104   1.4640  -1.0000  -1.0000   0.0000
82    ! Nr of angles;at1;at2;at3;Thetao,o;ka;kb;pv1;pv2
 1  1  1  74.0317  32.2712   0.9501   0.0000   0.1780  10.5736   1.0400
 1  1  2  70.6558  14.3658   5.3224   0.0000   0.0058   0.0000   1.0400
 2  1  2  76.7339  14.4217   3.3631   0.0000   0.0127   0.0000   1.0400
 1  2  2   0.0000   0.0000   6.0000   0.0000   0.0000   0.0000   1.0400
 1  2  1   0.0000   3.4110   7.7350   0.0000   0.0000   0.0000   1.0400
 2  2  2   0.0000  27.9213   5.8635   0.0000   0.0000   0.0000   1.0400
 1  1  3  65.1700   8.0170   7.5000   0.0000   0.2028  10.0000   1.0400
 3  1  3  71.7582  26.7070   6.0466   0.0000   0.2000   0.0000   1.8525
```

1 1 4 65.4228 43.9870 1.5602 0.0000 0.2000 10.0000 1.8525

3 1 4 73.7046 23.8131 3.9811 0.0000 0.2000 0.0000 1.8525

4 1 4 65.6602 40.5852 1.8122 0.0000 0.2000 0.0000 1.8525

2 1 3 59.4426 17.6020 2.3044 0.0000 0.9699 0.0000 1.1272

2 1 4 71.0777 9.1462 3.4142 0.0000 0.9110 0.0000 1.0400

1 2 4 0.0000 0.0019 6.3000 0.0000 0.0000 0.0000 1.0400

1 3 1 72.1018 38.4720 1.3926 0.0000 0.4785 0.0000 1.2984

1 3 3 89.9987 44.9806 0.5818 0.0000 0.7472 0.0000 1.2639

1 3 4 70.3281 13.2989 7.7058 0.0000 0.7472 0.0000 1.2639

3 3 3 84.2807 24.1938 2.1695 -10.0000 0.7472 0.0000 1.2639

3 3 4 84.2585 44.1039 0.9185 0.0000 0.7472 0.0000 1.2639

4 3 4 74.2312 25.7005 4.3943 0.0000 0.7472 0.0000 1.2639

1 3 2 89.0416 36.9460 0.4569 0.0000 2.7636 0.0000 2.0494

2 3 3 81.1709 4.2886 6.5904 0.0000 3.0000 0.0000 1.2618

2 3 4 75.9203 44.9675 0.8889 0.0000 3.0000 0.0000 1.2618

2 3 2 82.2020 12.7165 3.9296 0.0000 0.2765 0.0000 1.0470

1 4 1 68.3788 18.3716 1.8893 0.0000 2.4132 0.0000 1.3993

1 4 3 86.5585 37.6814 1.1611 0.0000 1.7325 0.0000 1.0440

1 4 4 74.4818 12.0954 7.5000 0.0000 1.7325 0.0000 1.0440

3 4 3 78.5850 44.3389 1.3239 -19.2266 1.7325 40.0000 1.0440

3 4 4 77.6245 32.0866 1.8889 -0.9193 1.7325 0.0000 1.0440

4 4 4 66.4718 15.9087 7.5000 0.0000 1.7325 0.0000 1.0440

1 4 2 90.0000 33.6636 1.1051 0.0000 0.2638 0.0000 1.1376

2 4 3 83.8493 44.9000 1.3580 0.0000 0.5355 0.0000 2.5279

2 4 4 78.7452 24.2010 3.7481 0.0000 0.5355 0.0000 2.5279

2 4 2 55.8679 14.2331 2.9225 0.0000 0.2000 0.0000 2.9932

1 2 3 0.0000 0.0019 6.0000 0.0000 0.0000 0.0000 1.0400

1 2 4 0.0000 0.0019 6.0000 0.0000 0.0000 0.0000 1.0400

1 2 5 0.0000 0.0019 6.0000 0.0000 0.0000 0.0000 1.0400

3 2 3 0.0000 0.0019 6.0000 0.0000 0.0000 0.0000 1.0400

3 2 4 0.0000 0.0019 6.0000 0.0000 0.0000 0.0000 1.0400

4 2 4 0.0000 0.0019 6.0000 0.0000 0.0000 0.0000 1.0400

2 2 3 0.0000 0.0019 6.0000 0.0000 0.0000 0.0000 1.0400

2 2 4 0.0000 0.0019 6.0000 0.0000 0.0000 0.0000 1.0400

1 1 5 74.4180 33.4273 1.7018 0.1463 0.5000 0.0000 1.6178

1 5 1 79.7037 28.2036 1.7073 0.1463 0.5000 0.0000 1.6453

2 1 5 63.3289 29.4225 2.1326 0.0000 0.5000 0.0000 3.0000

1 5 2 85.9449 38.3109 1.2492 0.0000 0.5000 0.0000 1.1000

1 5 5 85.6645 40.0000 2.9274 0.1463 0.5000 0.0000 1.3830

2 5 2 83.8555 5.1317 0.4377 0.0000 0.5000 0.0000 3.0000

2 5 5 97.0064 32.1121 2.0242 0.0000 0.5000 0.0000 2.8568

6 6 6 69.5456 21.6861 1.4258 0.0000 -0.2101 0.0000 1.3241

2 6 6 75.8168 21.6786 1.0588 0.0000 2.5179 0.0000 1.0400

2 6 2 78.5939 20.9272 0.8580 0.0000 2.8421 0.0000 1.0400

3 6 6 70.1016 5.3781 1.3167 0.0000 2.1459 0.0000 1.0400

2 6 3 73.6706 6.7092 3.7625 0.0000 0.8613 0.0000 1.0400

3	6	3	90.2344	7.7833	1.7464	0.0000	0.7689	0.0000	1.0400
6	3	6	25.0715	3.6526	0.3180	0.0000	4.1125	0.0000	1.0400
3	3	6	73.4663	25.0761	0.9143	0.0000	2.2466	0.0000	1.0400
2	3	6	63.6634	10.0346	2.6680	0.0000	1.6982	0.0000	1.0400
1	3	6	53.6634	15.7193	2.7680	0.0000	1.6982	0.0000	1.0400
2	2	6	0.0000	47.1300	6.0000	0.0000	1.6371	0.0000	1.0400
6	2	6	0.0000	31.5209	6.0000	0.0000	1.6371	0.0000	1.0400
3	2	6	0.0000	31.0427	6.5625	0.0000	1.6371	0.0000	1.0400
2	2	5	0.0000	0.0019	6.0000	0.0000	0.0000	0.0000	1.0400
1	1	6	72.5239	22.3583	2.0393	0.0000	1.0031	0.0000	1.0400
6	1	6	75.3369	18.9270	2.0703	0.0000	1.0031	0.0000	1.0400
1	6	1	69.3369	18.9270	2.1333	0.0000	1.0031	0.0000	1.0400
1	6	3	69.3004	18.9710	2.1533	0.0000	1.0031	0.0000	1.0400
1	6	6	69.3369	19.6964	2.0703	0.0000	1.0031	0.0000	1.0400
2	1	6	72.5949	10.9851	1.4246	0.0000	1.0000	0.0000	1.0400
1	6	2	72.5949	14.8347	2.4952	0.0000	1.0000	0.0000	1.0400
4	6	6	0.0000	30.0000	6.0000	0.0000	1.0000	0.0000	1.0400
4	6	4	74.2811	10.5525	2.0350	0.0000	0.9925	0.0000	1.0693
3	6	4	77.5533	10.2000	2.0100	0.0000	0.9900	0.0000	1.0500
6	4	6	76.5000	10.2000	2.0200	0.0000	1.0050	0.0000	1.0300
2	6	4	70.5000	10.0357	1.2043	0.0000	1.0151	0.0000	1.0388
2	4	6	70.5000	10.0250	2.0067	0.0000	1.0050	0.0000	1.0500
4	4	6	77.5000	10.2055	2.0200	0.0000	0.9900	0.0000	1.0400

```
 3  4  6  77.0000  10.0000   2.0000   0.0000   1.0000   0.0000   1.0400
 4  3  6  77.0000  10.0000   2.0000   0.0000   1.0000   0.0000   1.0400
 4  2  6   0.0000  20.0000   2.0000   0.0000   1.0000   0.0000   1.0400
 3  1  6  71.5949  10.8121   2.5256   0.0000   1.0000   0.0000   1.0400
 1  2  6   0.0000  10.0000   2.0000   0.0000   1.0000   0.0000   1.0400
35    ! Nr of torsions;at1;at2;at3;at4;;V1;V2;V3;V2(BO);vconj;n.u;n
 1  1  1  1   0.0000  48.4194   0.3163  -8.6506  -1.7255   0.0000   0.0000
 1  1  1  2   0.0000  63.3484   0.2210  -8.8401  -1.8081   0.0000   0.0000
 2  1  1  2   0.0000  45.2741   0.4171  -6.9800  -1.2359   0.0000   0.0000
 0  1  2  0   0.0000   0.0000   0.0000   0.0000   0.0000   0.0000   0.0000
 0  2  2  0   0.0000   0.0000   0.0000   0.0000   0.0000   0.0000   0.0000
 0  1  3  0   1.7254  86.0769   0.3440  -4.2330  -2.0000   0.0000   0.0000
 0  2  3  0   0.0000   0.1000   0.0200  -2.5415   0.0000   0.0000   0.0000
 0  3  3  0   1.2314 116.5137   0.5599  -4.1412   0.0000   0.0000   0.0000
 0  1  4  0  -1.3258 149.8644   0.4790  -7.1541  -2.0000   0.0000   0.0000
 0  2  4  0   0.0000   0.1000   0.0200  -2.5415   0.0000   0.0000   0.0000
 0  3  4  0   1.3168  57.0732   0.2679  -4.1516  -2.0000   0.0000   0.0000
 0  4  4  0   2.0000  75.3685  -0.7852  -9.0000  -2.0000   0.0000   0.0000
 0  1  1  0   0.0930  18.6070  -1.3191  -9.0000  -1.0000   0.0000   0.0000
 4  1  4  4  -2.0000  20.6655  -1.5000  -9.0000  -2.0000   0.0000   0.0000
 0  1  5  0   4.0885  78.7058   0.1174  -2.1639   0.0000   0.0000   0.0000
 0  5  5  0  -0.0170 -56.0786   0.6132  -2.2092   0.0000   0.0000   0.0000
 0  2  5  0   0.0000   0.0000   0.0000   0.0000   0.0000   0.0000   0.0000
```

0 6 6 0 0.0000 0.0000 0.1200 -2.4426 0.0000 0.0000 0.0000

0 2 6 0 0.0000 0.0000 0.1200 -2.4847 0.0000 0.0000 0.0000

0 3 6 0 0.0000 0.0000 0.1200 -2.4703 0.0000 0.0000 0.0000

0 4 6 0 0.0000 0.0000 0.0000 -2.4426 0.0000 0.0000 0.0000

1 1 3 3 1.2707 21.6200 1.5000 -9.0000 -2.0000 0.0000 0.0000

1 3 3 1 -1.8804 79.9255 -1.5000 -4.1940 -2.0000 0.0000 0.0000

3 1 3 3 -2.0000 22.5092 1.5000 -8.9500 -2.0000 0.0000 0.0000

1 4 4 3 0.1040 70.1152 0.5284 -3.5026 -2.0000 0.0000 0.0000

1 1 3 4 1.2181 119.6186 -1.5000 -7.0635 -2.0000 0.0000 0.0000

2 1 3 4 -2.0000 156.6604 1.1004 -7.3729 -2.0000 0.0000 0.0000

1 3 4 3 2.0000 96.6281 -1.5000 -3.8076 -2.0000 0.0000 0.0000

1 1 4 2 -2.0000 147.2445 -1.5000 -7.0142 -2.0000 0.0000 0.0000

1 1 4 3 -2.0000 47.8326 -1.5000 -9.0000 -2.0000 0.0000 0.0000

2 3 4 3 -0.2997 152.9040 -1.5000 -4.4564 -2.0000 0.0000 0.0000

2 4 4 3 0.1040 70.1152 0.5284 -3.5026 -2.0000 0.0000 0.0000

6 1 3 4 2.0000 70.2461 2.0000 -3.0635 -2.0000 0.0000 0.0000

3 1 6 1 5.0000 80.6070 5.0000 -3.0000 -2.0000 0.0000 0.0000

1 3 6 1 1.0000 80.6070 1.0000 -3.0000 -2.0000 0.0000 0.0000

9 ! Nr of hydrogen bonds;at1;at2;at3;Rhb;Dehb;vhb1

3 2 3 2.1845 -2.3549 3.0582 19.1627

3 2 4 1.7058 -3.8907 3.0582 19.1627

4 2 3 1.8738 -3.5421 3.0582 19.1627

4 2 4 1.8075 -4.1846 3.0582 19.1627

3	2	5	2.6644	-3.0000	3.0000	3.0000
4	2	5	4.0476	-3.0000	3.0000	3.0000
5	2	3	2.1126	-4.5790	3.0000	3.0000
5	2	4	2.2066	-5.7038	3.0000	3.0000
5	2	5	1.9461	-4.0000	3.0000	3.0000

VITAE

FARZIN RAHMANI

Department of Chemical Engineering

School of Engineering, University of Mississippi

134 Anderson, University, MS 38677-1848

Phone (Office): (662) 915-7023 Phone (Cell): (662) 801-2421

E-mail: frahmani@go.olemiss.edu

EDUCATION

01/2015-Present

Ph.D. Candidate in Chemical Engineering. University of Mississippi (Ole Miss), Oxford, Mississippi, United States.

Dissertation: "Reactive Molecular Dynamics Simulation of Materials in Extreme Environments."

09/2011-11/2013

Advisor: Sasan Nouranian (Ph.D., Mississippi State University, 2011)

Master of Science in Polymer Engineering (Polymer Industries Branch). Amirkabir University of Technology (Tehran Polytechnic), Tehran, Iran.

Thesis: "Investigation on the Stability of Graphene in an Aqueous Medium via Molecular Dynamics Simulation."

Advisors: Farhad Sharif (Ph.D., McMaster University) and Hormoz Eslami (Ph.D., McMaster University)

Bachelor of Science in Polymer Engineering (Polymer Industries Branch). Amirkabir University of Technology (Tehran Polytechnic), Tehran, Iran.

Thesis: "Investigation on the Modification of Polylactic acid (PLA) Toughness by Blending with Ethylene Vinyl Acetate (EVA)."

Advisor: Hamid Garmabi (Ph.D., McGill University, 1997)

ACADEMIC APPOINTMENTS

01/2015-present

Teaching Assistant. Department of Chemical Engineering, University of Mississippi, Oxford, Mississippi, United States.

Courses: Plant Design II, Introduction to Chemical Engineering I, Reactor Design, Fluid Dynamics and Heat Transfer, Advanced Transport Phenomena and II, Process Control and Safety

Teaching Assistant. Department of Polymer Engineering and Color Technology, University of Amirkabir, Tehran, Iran.

Courses: Fluid Mechanics, Thermodynamics

HONORS AND AWARDS

- Ph.D. Dissertation Fellowship Award (Spring 2018)
- Best Graduate Research Award, American Chemical Society (ACS), Local University of Mississippi Chapter (2017)
- Summer Graduate Research Assistantship, University of Mississippi (Summer 2017)

PUBLICATIONS:

PEER-REVIEWED JOURNAL PUBLICATIONS (8)

2018

1. **Rahmani, F.,** Jeon, J., Jiang, S., and Nouranian, S. "Melting and Solidification Behavior of Cu/Al and Ti/Al Bimetallic Core/Shell Nanoparticles During Additive Manufacturing by Molecular Dynamics Simulation," *Journal of Nanoparticle Research* (2018) (Under Review).

2017

2. Khakpay, A., **Rahmani, F.**, Nouranian, S., and Scovazzo, P. "Molecular Insights on the CH_4/CO_2 Separation in Nanoporous Graphene and Graphene Oxide Separation Platforms: Adsorbents versus Membranes," *The Journal of Physical Chemistry C* **121**(22) (2017): 12308-12320. DOI: 10.1021/acs.jpcc.7b03728

3. Li, X., Al-Ostaz, A., Jaradat, M., **Rahmani, F.**, Nouranian, S., Rushing, G., Manasrah, A., Alkhateb, H., Finckenor, M., and Lichtenhan, J. "Substantially Enhanced Durability of Polyhedral Oligomeric Silsesquioxane-Polyimide Nanocomposites Against Atomic Oxygen Erosion," *European Polymer Journal* **92** (2017): 233-249. DOI: 10.1016/j.eurpolymj.2017.05.004
4. **Rahmani, F.**, Nouranian, S., Li, X., and Al-Ostaz, A. "Reactive Molecular Simulation of the Damage Mitigation Efficacy of POSS-, Graphene-, and Carbon Nanotube-Loaded Polyimide Coatings Exposed to Atomic Oxygen Bombardment," *ACS Applied Materials and Interfaces* **9**(14) (2017): 12802-12811. DOI: 10.1021/acsami.7b02032
5. **Rahmani, F.**, Mahdavi, M., Nouranian, S., and Al-Ostaz, A. "Confinement Effects on the Thermal Stability of Poly(ethylene oxide)/Graphene Nanocomposites: A Reactive Molecular Dynamics Simulation Study," *Journal of Polymer Science, Part B: Polymer Physics* **55**(13) (2017): 1026-1035. DOI: 10.1002/polb.20170092
6. **Rahmani, F.**, Nouranian, S., Madavi, M., and O'Haver, J.H. "A Fundamental Investigation of the Surfactant-Stabilized Single-Walled Carbon Nanotube/Epoxy Resin Suspensions by Molecular Dynamics Simulation," *Materials Research Express* **4**(1) (2017): 015016. DOI: 10.1088/2053-1591/aa5465

2016

7. **Rahmani, F.**, Nouranian, S., Mahdavi, M., and Al-Ostaz, A. "Molecular Simulation Insights on the In Vacuo Adsorption of Amino Acids on Graphene Oxide Surfaces with Varying Surface Oxygen Densities," *Journal of Nanoparticle Research* **18**(11) (2016): 320. DOI: 10.1007/s11051-016-3631-7

8. Mahdavi, M., **Rahmani, F.**, and Nouranian, S. "Molecular Simulation of pH-dependent Diffusion, Loading, and Release of Doxorubicin in Graphene and Graphene Oxide Drug Delivery Systems," *Journal of Materials Chemistry B* **4** (2016): 7441-7451. DOI: 10.1039/C6TB00746E

CONFERENCE PRESENTATIONS (10)

2017

1. **Rahmani, F.,** Khakpay, A., Nouranian, S., and Scovazzo, P. "CH_4 and CO_2 Transport Properties through Nanoporous Graphene and Graphene Oxide Membranes: A Molecular Dynamics Simulation Study," The 2017 Annual Meeting of the American Institute of Chemical Engineers (AIChE), Minneapolis, MN, United States, October 29-November 3 (2017).
2. Nouranian, S., **Rahmani, F.**, Mahdavi, M., and Al-Ostaz, A. "Mitigation of Atomic Oxygen Attack to Spacecraft Composite Structures: A Fundamental Investigation Using Reactive Molecular Dynamics Simulation," TMS 2017, The 146th Annual Meeting and Exhibition, San Diego, CA, United States, February 26-March 2 (2017).

2016

3. **Rahmani, F.**, Nouranian, S., and Mahdavi, M. "A Reactive Molecular Dynamics Simulation of the Thermal Decomposition in Graphene-Reinforced Polyethylene Oxide," The 2016 Annual Meeting of the American Institute of Chemical Engineers (AIChE), San Francisco, CA, United States, November 13-18 (2016).

4. **Rahmani, F.**, Nouranian, S., and Mahdavi, M. "A Computational Investigation of the Surfactant-Mediated Carbon Nanotube Stabilization in a Liquid Epoxy Resin," The 2016 Annual Meeting of the American Institute of Chemical Engineers (AIChE), San Francisco, CA, United States, November 13-18 (2016).
5. Mahdavi, M., Nouranian, S., and **Rahmani, F.** "An Experimental and Computational Study of the Surface Chemistry Effects in the TiO_2 Grafting of Graphene Oxide," The 2016 Annual Meeting of the American Institute of Chemical Engineers (AIChE), San Francisco, CA, United States, November 13-18 (2016).
6. Nouranian, S., **Rahmani, F.**, McFall, H., and Zosel, Z. "Molecular Dynamics Simulation of Carbon Nanotube Stabilization in an Epoxy Resin Using Cationic and Anionic Surfactants," NanoWorld Conference 2016, Boston, MA, United States, April 4-6 (2016).

2015

7. Mahdavi, M., **Rahmani, F.**, and Nouranian, S. "Graphene Oxide Nanocarrier for Doxorubicin Anticancer Drug, a Molecular Dynamics Simulation Study," The 2015 Annual Meeting of the American Institute of Chemical Engineers (AIChE), Salt Lake City, UT, United States, November 8-13 (2015).
8. **Rahmani, F.**, Nouranian, S., and Zajforoushan Moghaddam, S. "Molecular Dynamics Simulation of Amphiphilic Graphene Oxide as a Tunable Colloidal Surfactant in Oil/Water Mixtures." The 2015 Annual Meeting of the American Institute of Chemical Engineers (AIChE), Salt Lake City, UT, United States, November 8-13 (2015).
9. **Rahmani, F.**, Khalkhali, R., Sharif, F., and Nouranian, S. "Stabilization of Graphene in Water-Ethanol Mixture by Molecular Dynamics Simulation." The 15th Southern School on Computational Chemistry and Materials Science Conference, Jackson State University,

MS, United States, July 23-24 (2015).

2011

10. **Rahmani, F.**, Beheshti, M.H., and Javadi, S. "The Effect of Clay Content on Bonding Properties of Novolak Adhesives." Congress of the Polymer Processing Society (PPS2011), Kish Island, Iran, November 15-17 (2011).

CONFERENCE POSTERS (2)

1. Khakpay, A., **Rahmani, F.,** Nouranian, S., Scovazzo, P. "Molecular Insights on the Reverse-Selectivity Potential of Room Temperature Ionic Liquid Membranes." Abstract submitted to the 2017 Annual Meeting of the American Institute of Chemical Engineers (AIChE), Minneapolis, MN, U.S.A. October 29-November 3 (2017).
2. **Rahmani, F.,** Khakpay, A., Nouranian, S., Scovazzo, P. "Molecular Dynamics Simulation of Room Temperature Ionic Liquid Membranes for CO_2/CH_4 and CO_2/N_2 Separations." Abstract submitted to the 2017 Annual Meeting of the American Institute of Chemical Engineers (AIChE), Minneapolis, MN, U.S.A. October 29-November 3 (2017).

OTHER PRESENTATIONS (1)

1. **Rahmani, F.** "Smart Materials Save Lives," The Three-Minute Dissertation (3MT), University of Mississippi, October 26 (2017).

PROFESSIONAL SERVICE/MENTORING ACTIVITIES

- Reviewer for the Journal of Nanoparticle Research
- Mentored Jungmin Jeon, Mechanical Engineering Master's student, University of

Mississippi

- Mentoring Hatem Almasaeid, Civil Engineering Ph.D. student, University of Mississippi (2017-present)
- Mentored Alex Brown, Chemical Engineering undergraduate student, University of Mississippi (2017)
- Mentored Amir Khakpay, Chemical Engineering Ph.D. student, University of Mississippi (2017)
- Mentored Haley McFall and Zachary Zosel, Chemical Engineering undergraduate students, University of Mississippi (2016)
- Mentored Mina Mahdavi, Chemical Engineering Ph.D. student, University of Mississippi (2015-2017)

PROFESSIONAL SKILLS

- Proficient in Atomic Force Microscopy (AFM), tensile testing, compression molding, and plastics extrusion, (Reactive)-Molecular Dynamics Simulation, Finite Element